Article

# Oxidization of Reduced Graphene Oxide *via* Cellular Redox Signaling Modulates Actin-Mediated Neurotransmission

Yiyuan Kang, Jia Liu, Suhan Yin, Yanping Jiang, Xiaoli Feng, Junrong Wu, Yanli Zhang, Aijie Chen, Yaqing Zhang, and Longquan Shao

*ACS Nano*, **Just Accepted Manuscript** • DOI: 10.1021/acsnano.9b08078 • Publication Date (Web): 14 Feb 2020

# Oxidization of Reduced Graphene Oxide *via* Cellular Redox Signaling Modulates Actin-Mediated Neurotransmission

Yiyuan Kang[†,‡,#], Jia Liu[†,#], Suhan Yin[†], Yanping Jiang[†], Xiaoli Feng[†], Junrong Wu[†], Yanli Zhang[†], Aijie Chen[†],Yaqing Zhang[†], Longquan Shao[†,‡,*]

[†] Nanfang Hospital, Southern Medical University, Guangzhou 510515, China

[‡] Guangdong Provincial Key Laboratory of Construction and Detection in Tissue Engineering, Guangzhou 510515, China

*To whom correspondence should be addressed: Shao Longquan.

E-mail addresses: shaolongquan@smu.edu.cn

[#]These authors contribute equally to this work.

**Abstract**

Neurotransmission is the basis of brain functions, and controllable neurotransmission tuning constitutes an attractive approach for interventions in a wide range of neurologic disorders and for synapse-based therapeutic treatments. Graphene-family nanomaterials (GFNs) offer promising advantages for biomedical applications, particularly in neurology. Our study suggests that reduced graphene oxide (rGO) serves as a neurotransmission modulator and reveals that the cellular oxidation of rGO plays a crucial role in this effect. We found that rGO could be oxidized *via* cellular reactive oxygen species (ROS), as evidenced by an increased number of oxygen-containing functional groups on the rGO surface. Cellular redox signaling, which involves NADPH oxidases and mitochondria, was initiated and subsequently intensified rGO oxidation. The study further shows that the blockage of synaptic vesicle docking and fusion induced through a disturbance of actin dynamics is the underlying mechanism through which oxidized rGO exerts depressant effects on neurotransmission. Importantly, this depressant effect could be modulated by restricting the cellular ROS levels and stabilizing the actin dynamics. Taken together, our results identify the complicated biological effects of rGO as a controlled neurotransmission modulator and can provide helpful information for the future design of graphene materials for neurobiological applications.

**Keywords:** graphene, reduced graphene oxide, redox signaling, neurotransmission, actin filament

Graphene-family nanomaterials (GFNs) are highly versatile 2D nanomaterials that have been widely adopted in many domains of science and technology, including biomedical applications. Recently, GFNs have been regarded as one of the most suitable classes of materials for neurological applications due to their special electrochemical properties, high surface area, mechanical strength and high flexibility. GFN-based products, such as neuronal implants or biodevices, have shown great advantages for the recording and modulation of neural activity and might overcome the current technical limitations associated with the treatment of various pathologies ranging from neuro-oncology to neuroregeneration.[1-4]

In addition to the external implantation approach, GFNs, particularly graphene oxide (GO), can also be applied in an injectable pattern for the tuning of synaptic transmission.[5,6] This capability of GO is mainly attributed to its high affinity for neuronal membranes, which potentially affects numerous membrane activities.[7,8] However, some concerns have gradually been raised, and these include the uncontrolled intervention pathway and the lower biocompatibility of GO compared with those of graphene and reduced graphene oxide (rGO),[9,10] which might lead to irreversible damage to the nervous system. Moreover, the complicated biological signaling processes underlying the effects of GO need further elucidation. Thus, there is an urgent need for the development of a GFN-based controllable neurotransmission modulator with enhanced biological safety, and its intrinsic mechanism should be investigated in detail.

As another widely used GFN obtained by reducing GO, rGO exhibits different

physicochemical properties from GO, such as higher hydrophobicity, better biocompatibility, and preferable electrical conductivity, which is mainly due to its lower degree of oxidation. Generally, the transformation process between rGO and GO can be induced through the use of strong oxidants and reductants.[11,12] Although the recent studies have reported that rGO can be transformed to GO in an rGO-bacteria coculture system without any foreign oxidants,[13,14] the biological mechanisms have not been clearly revealed. We hypothesize that this biological oxidation process of rGO provides a potential approach for discovering controlled neurotransmission modulators that exhibit good compatibility. In this study, we revealed that rGO can be oxidized under coculture with neuronal cells, where cellular reactive oxygen species (ROS) are the principal contributor.

Cellular ROS are mainly generated from intracellular redox signaling, including NADPH oxidases (NOXs) and mitochondria, which is the important factor for maintaining cellular physiological activity. On the basis of these considerations, we verified that rGO could be oxidized *via* cellular ROS, transforming rGO into oxidized rGO. Furthermore, we detected the alterations in actin-mediated synapse exocytotic function induced by oxidized rGO in neuronal cells (PC12 cell line and primary cortical neurons). Parameters such as NOXs activation, mitochondrial dysfunction and actin dynamic disturbance were studied. Our results revealed important oxidation loops between cellular redox signaling molecules and rGO, and suggested that a controlled cellular redox system could be utilized for rGO to modulate neurotransmission, indicating opportunities for controllable neuromodulatory applications in the future.

## Results and Discussion

### rGO Oxidization Occurs under Coculture with Neuronal Cells.

The atomic force microscopy (AFM) results showed that rGO was a single-layer nanosheet with a height of approximately 0.6 nm and that its surface was flowing and smooth (Figure 1A). The dispersity of rGO was determined by zeta potential and DLS measurements. rGO nanosheets showed more agglomeration in complete culture medium (189.9 ± 31.1 nm) than in deionized water (98.4 ± 21.3 nm). The zeta potential of rGO in deionized water was -12.5 ± 4.7 mV (Table 1). Furthermore, the metallic impurity content of a pristine rGO sample was assessed by inductively coupled plasma mass spectrometry (ICP-MS), which showed that the rGO used in this study is highly pure, with a metallic impurity content much lower than that of GFNs used in other studies (Table S1).[15,16] X-ray diffraction (XRD) was performed to assess the crystal structure, and the data showed that the $2\theta$ peak of rGO was 20.23°, which corresponded to an interlayer distance of d = 4.38 Å. indicating that rGO was well reduced from GO (11.71°, d = 7.56 Å) (Figure S1A).

X-ray photoelectron spectroscopy (XPS), which allows significant surface-sensitive and detailed speciation of the oxide, was used to quantify the functional groups on the surface of rGO. The C1s peak in the XPS data was fitted with Gaussian-Lorentzian curves to quantitatively differentiate the carbon moieties: C–C (284.6 eV), C–OH (285.8 eV), C–O–C (286.6 eV) and C=O (288.2 eV). Based on the XPS survey (Figure S3) and areas of these peaks, the carbon-to-oxygen (C/O) ratio and percentages of the different groups in rGO can be obtained.[17] We found that the total oxygen percentage of the pristine rGO

sample was only 11.40% and that the C/O ratio was 7.77, which showed that rGO was effectively reduced compared with GO (Figure S1).[18] The percentages of C=O, C–O–C and C–OH were 4.24, 5.32 and 1.84% respectively (Table 2). We further collected rGO materials after coculture with PC12 cells, a typical neuronal cell model, and detected the percentage of oxygen-containing groups. The concentration of rGO employed throughout the study was 20 $\mu$g/mL, which is a nontoxic concentration, as evidenced by cell viability measurements. For comparison, the cell viability of GO was also measured, and the results showed that GO exerted stronger toxic effects (Figure S1E and S2). The total percentage of oxygen-containing groups on the rGO surface increased to almost 19.16% after 3 h of coculture with neuronal cells, accompanied by a C/O ratio of 4.22. Specifically, the percentage of C–OH groups on the rGO surface after coculture with neuronal cells for 30 min, 1 h and 3 h gradually increased to 5.74, 7.63 and 9.41%, respectively. However, the percentages of the C–O–C and C=O groups were maintained at a stable level (Figure 1B and Table 2). These data indicated that the graphene structure was clearly changed in the rGO-neuronal cell coculture system, mainly manifested as the generation of hydroxyl groups attached to the carbon backbone.

We also verified this oxidation process *via* Raman spectroscopy, which is a powerful tool for identifying the presence of $sp^2$ carbon on the surface of GFNs. $sp^2$ carbon provides two clear signatures of rGO in the Raman spectrum through the first-order peaks at 1347.6 $cm^{-1}$ and 1585.5 $cm^{-1}$, which are named the D and G bands, respectively (Table 1). The stretching of all $sp^2$ carbon pairs in both rings and chains leads to the so-called G (graphitic)

mode, whereas the breathing modes of $sp^2$ atoms in rings lead to the D (defect) mode, which indicates the presence of disorder in $sp^2$ carbon rings induced mainly by graphene defects and edges. In this study, two main indexes, the ratio of the area of D to that of G bands ($D/G_{(area)}$) and the full width at half maximum (FWHM) of the G band, were used to characterize the level of graphene surface defects, which include oxygen-containing surface functional groups as well as structural defects.[13,19] Our data showed that the $D/G_{(area)}$ ratio of pristine rGO was 1.50 and that the FWHM of the G band was 59.07 $cm^{-1}$. The coculture of rGO with PC12 cells for 3 h increased the $D/G_{(area)}$ ratio and FWHM of the G band to 1.95 and 97.97 $cm^{-1}$, respectively. These data indicated that the oxidation degree of rGO increased in our rGO-neuronal cell coculture system (Figure 1C).

GFNs are $sp^2$ lattice materials that exhibit strong stability on their surface. However, it has been reported that the oxygen-containing functional groups (electron-rich carbonyl groups (C=O))[20] and heteroatom/defect sites in the graphene structure (zigzag edges, nonhexagonal units and vacancy defects) exhibit more active performance[21,22] and thus GFNs have some potential applications in various fields such as antimicrobial research.[23] Therefore, we suggested that these active sites could be oxidized *via* cellular oxidants, such as cellular-derived ROS, which were the main factor in the significant increase in the oxidation degree of rGO (Figure 1D). Our data further support our hypothesis. We found that the oxidation degree of rGO was decreased after coculture with neuronal cells in which ROS had been eliminated *via* N-acetylcysteine (NAC), a well-known membrane-penetrating antioxidant. The Raman spectrum data showed that coculture under these

conditions reduced the $D/G_{(area)}$ ratio and FWHM of the G band from 1.95 to 1.58 and from 97.97 $cm^{-1}$ to 67.71 $cm^{-1}$, respectively. The XPS data showed that the percentage of C–OH groups on the rGO surface also remained at a low level (3.17%) and that the C/O ratio was only 6.43 (Figure 1C and Table 2). These findings demonstrated that the elimination of ROS potently blocked the rGO oxidation process.

**Hydrogen Peroxide Mainly Contributes to the Biological Oxidation of rGO.**

The existence of a physiological concentration of ROS is beneficial for regulating normal cell functions and responding to various stimuli. Among a series of ROS (including superoxide anions, hydroxyl radicals (•OH) and hydrogen peroxide ($H_2O_2$)), $H_2O_2$ is the most well-known and long-lived ROS present in almost all mammalian cells and can freely diffuse between the inside and outside of the cell membrane; in contrast, other oxygen free radicals are short-lived (superoxide anions: ~5 s, •OH: ~2 $\mu$s).[24] Therefore, was cellular $H_2O_2$ the main substance mediating the rGO oxidation process?

To elucidate the reaction process and the intrinsic mechanism in detail, we applied density functional theory (DFT) with a solvation model to calculate this reaction process. Two possible rGO sites were considered: reaction sites on the graphene surface around the –COC– groups and reaction sites at the edge of graphene around the –COOH groups. As shown in Figure 2A-B, both pathways decompose $H_2O_2$ and yield –OH attached to active sites on rGO, which is in good agreement with our XPS experimental results. After one $H_2O_2$ is decomposed into two –OH groups on the graphene surface or edge, a partial of •OH groups are desorbed from graphene. The dissociation adsorption energy of $H_2O_2$

around the –COC– groups on the graphene surface is -0.14 eV. Additionally, further desorption of the first and second •OH radicals is an endothermic process of 1.91 and 1.32 eV, respectively. At the edge of rGO, the dissociation adsorption energy of $H_2O_2$ is -1.17 eV, and the desorption energies of the first and second •OH radicals are 1.43 and 2.83 eV, respectively. According to the energy profile, the edge is more active than the rGO surface, where $H_2O_2$ is most easily decomposed and generate stronger adsorption of –OH. This phenomenon occurs because the C–H group at the edge prefers to adopt the –OH group and the adjacent –COOH group can also be involved in the hydrogen bonding network, which is consistent with the previous findings that –COOH groups at the edges/defects of GFNs are rich in electrons and can coordinate redox reactions.[25]

The adsorption of $H_2O_2$ and the subsequent –OH groups formation on rGO also lead to charge transfer from rGO to the –OH group, which changes the charge state of O from -1 |e| to -1.71 |e|, as demonstrated through a Bader charge analysis. The electronic properties of $H_2O_2$ adsorbed on rGO are detailed in Figure S4, which provides the projected density of states on C and O. The density of states showed a small gap of approximately 0.3 eV in rGO. However, two new peaks appear at the Fermi level due to the dissociative adsorption of $H_2O_2$ and charge transfer. This observation shows that rGO is a good electron buffer for the redox reaction, consistent with a previously suggested mechanism that electron transfer occurs from the top of the valence band of GFNs to the lowest unoccupied molecular orbital of $H_2O_2$,[26] and this electron transfer drives the $H_2O_2$ decomposition. In addition, the C–C bond length under the –OH group is elongated to 1.61 Å from 1.42 Å,

indicating a conversion from a double bond to a single bond. Furthermore, one •OH desorption from graphene plane was viable due to the high electron transfer of rGO, and the energy derived from $H_2O_2$ decomposition was thermodynamically favored as well. However, a relatively higher energy was required making it's difficult for the second •OH desorption from rGO plane surface. We suggested that, the low oxygen containing groups and high structural defects on rGO surface can affect the electron mobility and the subsequently electron transfer with the active species,[25] leading to some –OH attachment after $H_2O_2$ decomposition and rGO oxidation finally.

To verify the consequences obtained by DFT, we detected the generation of •OH after the coculture of rGO with $H_2O_2$. Intriguingly, we found that rGO or $H_2O_2$ alone did not generate any radicals, as shown by the electron spin resonance (ESR) data, but the coculture of $H_2O_2$ and rGO resulted in the generation of •OH (Figure 2C). Furthermore, the XPS data showed that the total percentage of oxygen-containing groups on the rGO surface increased to almost 16.26% after the coculture of $H_2O_2$ and rGO, and this increase was accompanied by an increase in the percentage of C–OH groups to 6.21 (Figure S5). These data strongly support the DFT calculation results. Based on these findings, we conclude that rGO can directly react with cellular-derived $H_2O_2$, leading to the oxidation of rGO and the reconstruction of its carbon structure.

**Oxidized rGO Induces Plasma Membrane Perturbation in Neuronal Cells.**

Many studies have suggested that rGO materials exhibit more hydrophobic interactions with the cell membrane than GO materials, mainly because they have fewer

oxygen-containing groups on their surface.[19] Mao[27] reported that more highly oxidized graphene materials possess stronger membrane disturbing abilities, leading to more graphene nanosheets piercing the cell membrane. Therefore, we determined whether the oxidation process of rGO is involved in its influence on membrane stability.

Our study isolated and identified primary cortical neurons (Figure S2) and observed direct contact between rGO and the plasma membrane *via* scanning electron microscopy (SEM). Representative SEM images showed that rGO directly adhered to or even pierced into the cell membrane of PC12 cells and primary neurons after treatment for 1 h (Figure 3A). Moreover, membrane lipid peroxidation, which manifested as a consistent increase in the green fluorescence of BIODIPY C11 dyes (a membrane lipid peroxidation sensor exhibiting a shift in fluorescence from red to green upon lipid peroxidation), readily occurred as early as 10 min after rGO treatment (Figure 3B-C). Notably, the observed high membrane affinity and oxidation ability of rGO were close to the GO-induced effects shown in Figure S1 and observed in other studies.[18,19,28] These data, accompanied by the our characterization results, proved that the redox reaction between $H_2O_2$ and rGO transforms the physicochemical properties of rGO to become more similar to those of GO.

To elucidate the role of oxidized rGO in these rGO-induced biological effects, we collected biologically oxidized rGO after coculture with PC12 cells for 3 h (*c*-rGO) and then detected the levels of membrane lipid peroxidation after *c*-rGO and pristine rGO (*p*-rGO) treatment. Before treatment, cellular ROS were eliminated *via* NAC to exclude their interference with the biological oxidation process. Our data showed that *c*-rGO induced a

higher lipid membrane peroxidation degree than *p*-rGO (Figure S6A-B). It's an interesting issue that *p*-rGO exhibited much weaker lipid peroxidation in a cellular environment without ROS than in a cellular environment with ROS. These results suggested that the oxidation process of rGO under coculture with cells was an important condition for the rGO-mediated induction of cell stress and other biological effects.

Because an increase in the concentration of oxygen-containing groups in GFNs indicates enhanced uptake efficiency,[29] the uptake of rGO was detected. We constructed FITC-labeled rGO nanosheets and observed FITC fluorescence in the cytoplasm, which indicates the internalization of rGO. The confocal microscopy observations were further substantiated by visualizing the cytoplasm localization *via* transmission electron microscopy (TEM). Moreover, we found that the side scatter (SSC), which represents the cell density, significantly increased in a time-dependent manner. The results reflected that rGO treatment induced a potent increase in the internal granularity of the neuronal cells, confirming the existence of internalized rGO (Figure S7).

The cellular ROS level was detected considering its crucial role in the oxidation of rGO. In both PC12 cells and primary neurons, the cellular ROS levels almost persistently increased from as early as 30 min, whereas a small decrease was observed after 3 h of rGO treatment. NAC mostly reversed the increase in ROS generation (Figure 3D). Importantly, the cellular uptake of rGO was reduced after NAC treatment, as evidenced by the decrease in SSCs and the increase in forward scatter (FSC) patterns, which is another flow cytometry-derived index representing the cell area (Figure 3E). These blockage effects of

NAC indicated that the elimination of cellular ROS inhibited rGO oxidation and increased the attachment of rGO to the cell membrane.

We then speculated whether rGO, particularly oxidized rGO, possesses the ability to modulate neurotransmission, which is strongly interlinked with membrane structural and functional stabilities. Synaptic currents, which represent single-cell synaptic activity, were recorded. Miniature excitatory postsynaptic currents (mEPSCs) are caused by the stochastic fusion of neurotransmitter vesicles at the presynaptic membrane, and their frequency is proportional to the number of synaptic contacts, representing the status of neurotransmission. Notably, our results showed that rGO significantly decreased the frequency and amplitude of mEPSCs and increased their rise time without affecting their decay time. These effects suggested that, similar to GO (Figure S1G), rGO significantly decreased neurotransmission in cortical neurons. Interestingly, these effects on excitatory transmission were significantly blocked after the elimination of cellular ROS (Figure 3F).

The above-mentioned data demonstrate that oxidized rGO exhibits higher affinity for the cell membrane and a depressant effect on excitatory neurotransmission. However, the cellular ROS concentration, which is precisely controlled at a basic level under normal conditions, is too low to cause this marked degree of rGO oxidation. We hypothesized that cellular redox signaling, which is the main biological origin of ROS, is involved and that its initiation can intensify the oxidation process.

**The rGO-Activated NOX Pathway Is One of the Main Sources of ROS Generation.**

To gain more insight into the condition of cellular redox signaling, the roles of NOX

enzymes were studied. NOXs are well-known sources of cellular ROS, and the most widely distributed isoforms in neuronal systems are NOX1, NOX2 and NOX4.[30,31] NOX2 consists of two membranous subunits, gp91$^{phox}$ (named NOX2 in this study), p22$^{phox}$, and a Rac1/2-containing cytoplasmic complex along with phosphorylated p67$^{phox}$, p47$^{phox}$, and p40$^{phox}$. Similarly, NOX1 forms a heterodimeric complex with p22$^{phox}$ and assembles with Rac1 plus NOXO1 (p47$^{phox}$ isoform) and NOXA1 (p67$^{phox}$ isoform) to form an active complex. NOX4 also requires p22$^{phox}$ but no other regulatory subunits and is constitutively active.

In general, varied expression levels and distributions of NOX subtypes exist in different mammalian cells. In our study, the detection of NOX protein levels showed that only the levels of NOX2 increased in PC12 cells and that only the levels of NOX1 significantly increased in cortical neurons (Figure 4A-B). The immunofluorescence results also supported these findings. In PC12 cells, increased NOX2 expression and distribution on the plasma membrane were observed. NOX1 was mainly located in the cortical neuron nucleus but could translocate to the cytoplasm and plasma membrane after rGO treatment (Figure 4C-D). Based on these observations, we subsequently verified the activation of NOX1 and NOX2 in primary neurons and PC12 cells separately.

The assembly of a Rac1/2-containing cytoplasmic complex with NOXs was the main piece of evidence used to indicate NOX enzyme activation. The coimmunoprecipitation (Co-IP) data obtained with PC12 cells showed that rGO treatment increased the levels of combined Rac2 (instead of Rac1) and NOX2 (Figure 4E and Figure S8A). Furthermore, we isolated the plasma membrane proteins after rGO treatment and found that p67$^{phox}$ and

p47$^{phox}$ were phosphorylated and translocated to the cell membrane together with Rac2 (Figure S8B). These results provide strong evidence demonstrating the generation of the NOX2 enzyme complex in PC12 cells. Whilst, to confirm the formation of the NOX1 activation complex in cortical neurons, the combination between Rac1 and NOX1 was revealed by Co-IP (Figure 4F). The membrane proteins were also isolated, and more NOXA1 and NOXO1 were translocated to the membrane after rGO treatment, which strongly confirmed the formation of NOX1 complex in cortical neurons (Figure 5A).

Most importantly, we evaluated whether NOXs were a major source of ROS in neuronal cells after rGO treatment. First, we constructed and screened siRNAs that effectively knocked down NOX2 and NOX1 expression in PC12 cells and cortical neurons, respectively. The data showed that NOX enzyme complexes generation on the plasma membrane and cellular ROS generation were inhibited after rGO treatment in siNOX-transfected neuronal cells (Figure 5B-C and Figure S9-10). Moreover, NOX-specific inhibitors were used to confirm the role of NOX1/2. Apo, an important NOX inhibitor, strongly inhibits all NOX species, whereas GKT137831 (GKT) and ML171 show selective inhibitory effects against NOX1/4 and NOX1, respectively. In PC12 cells, GKT and ML171 exerted few inhibitory effects on ROS generation, whereas Apo potently decreased ROS generation. The phosphorylation of p47$^{phox}$ was also significantly inhibited by the addition of Apo or NAC (Figure S8). In cortical neurons, the three NOX inhibitors, Apo, GKT and ML171, reduced the expression of NOX1 and inhibited the generation of ROS in cortical neurons (Figure 5D and Figure S10). These data directly confirmed the crucial

role of NOX2 and NOX1 in regulating rGO-induced ROS generation in PC12 cells and cortical neurons, respectively.

Altogether, these findings disclose the existence of an oxidation loop based on cellular NOXs activation: extracellular ROS first oxidize the attached rGO (as evidenced by the oxidation of rGO in the extracellular environment provided in Table 2), and the resulting oxidized rGO has higher affinity for the cell membrane than pristine rGO. Subsequently, the oxidized rGO activates the cellular NOX system to produce and release a higher level of cellular ROS, which in turn intensifies the oxidation of rGO (Figure 5E). Consistent with this proposal, NOXs activation was effectively blocked after inhibition of the rGO oxidation process by NAC. The oxidation of rGO was also potently blocked after NOX knockdown, as evidenced by the decrease in the oxidation degree detected by XPS (Figure S9D-E). Furthermore, one question regarding this proposed process that we subsequently investigated was whether oxidized rGO was a sufficient or even a necessary condition for NOX activation, and we used the above-mentioned experimental scheme for this investigation. We found that *c*-rGO showed more potent NOX2 activation ability than *p*-rGO in an environment without ROS, as evidenced by higher membrane protein levels of NOX2-related proteins. This experiment revealed that oxidized rGO played an important role in NOX2 activation, which then directly promoted this operative cycle (Figure S6C-D). Importantly, this oxidation loop implies a potential target for rGO as a controllable neurotransmission modulator. Specifically, if this oxidation loop is not terminated, additional rGO would be continuously oxidized, leading to further inhibition of

neurotransmission. Conversely, this neurotransmission modulator would not work very well after cellular redox signaling is concluded.

**rGO-Targeted Mitochondria Serve as Another Main Source of ROS Generation.**

Mitochondria also play a regulatory role in cellular redox signaling, and two processes constitute the main sources for mitochondria-derived ROS (mtROS) generation: mitochondrial inner membrane complexes I-III and mitochondrial matrix/inner membrane-bound dehydrogenases.[32,33] Importantly, our above-mentioned data showed that the ROS levels also increased to some extent at the late stage (>3 h) even after NOXs inhibition (Figure 5D and Figure S8C). We further detected whether the mitochondria were another important source of ROS.

In our study, rGO treatment for more than 3 h significantly affected the mitochondrial structure and function. The TEM results showed that rGO flakes could intertwine with the mitochondrial membrane or directly translocate into the mitochondrial matrix (Figure 6A). These interactions of rGO with mitochondria likely disrupted the intact membrane, which could directly affect the mitochondrial membrane potential (MMP) and inactive inner mitochondrial membrane complexes, particularly electron transport chain (ETC) complexes. We evaluated the changes in the MMP firstly. Tetramethylrhodamine ethyl ester (TMRE) was used to label mitochondria with normal MMP, and MitoTracker was simultaneously used to label all mitochondria. We found that the MMP was normal after rGO treatment for 1 h, but more mitochondria were not labeled with TMRE after 6 h of treatment, indicating depolarization of the MMP (Figure 6B and Figure S11). The activity

of ETC complexes, including complexes I-V, was then observed to considerably decrease after rGO treatment in a time-dependent manner. In addition, disruption of the mitochondrial respiratory chain led to blockage of ATP generation, as evidenced by a decrease in the cellular ATP levels (Figure 6C-D).

To confirm the role of mtROS in the redox system, we detected the generation of mtROS *via* MitoSOX, which is a mitochondria-targeted probe for ROS. The data showed that the mtROS levels were substantially elevated after rGO treatment for more than 3 h and that both NAC and MitoTEMPO (mTP, a mitochondria-targeted ROS scavenger) significantly eliminated the increase in mtROS. Importantly, the trend in mtROS generation was in accordance with the detected trend in the cellular ROS levels, which indicated that mtROS was one of the main sources of cellular ROS at the late stage after rGO treatment (>3 h) (Figure 6E-F). The TMRE levels were subsequently detected after the elimination of mitochondrial or total cellular ROS. We found that both mTP and NAC inhibited rGO-induced mitochondrial dysfunction to some extent and that NAC exerted a stronger inhibitory effect than mTP (Figure 6G). This result was attributed to the fact that the rGO oxidation process was blocked after NAC treatment, which directly decreased the cellular uptake of rGO and inhibited its direct contact with mitochondria. In contrast, mTP targeted the mitochondria, eliminated the surrounding cellular and intramitochondrial ROS, which is reportedly a main stimulator of mitochondrial redox signaling, and ultimately caused mitochondrial oxidative damage.[34] These data together demonstrated that the direct contact between rGO and existing cellular ROS jointly led to mitochondrial oxidative

damage.

Taken together, the findings indicate that mitochondria are another main source of cellular ROS, particularly at the late stage of rGO exposure. The oxidized rGO can directly contact and pierce into the mitochondrial membrane, which results in the induction of similar interaction effects between oxidized rGO and the cell membrane. Importantly, these subcellular interactions should be given more attention when applying GFNs in neurology. We believe that a small level of mitochondrial dysfunction is beneficial for cellular ROS generation and rGO oxidation because it results in limited damage to cellular metabolism. Therein, mTP, as a mitochondria-targeted ROS scavenger, can be applied to exert a protective effect on mitochondria.

**Oxidized rGO Disturbs Actin Dynamics.**

The actin cytoskeleton, which is the structural basis for numerous membrane activities, comprises a dynamic polymerization/depolymerization network. Many factors can regulate cytoskeleton dynamics, including physical stress and cellular oxidative effects.[35-37] We hypothesized that changes in the dynamics of actin filaments are the main drivers of the rGO-induced depression of neurotransmission. In this study, we found that rGO can directly contact the actin system, and typical actin dots (indicating the abnormal accumulation of actin monomers) were observed surrounding the contact sites in both cortical neurons and PC12 cells as soon as 1 h after treatment (Figure 7A). This finding suggested that the actin dynamics near the rGO contact sites were likely affected.

To reveal the detailed molecular mechanisms underlying actin dynamics, we

investigated some actin polymerization-related proteins, such as ARP2/3 and cortactin. Cofilin, a main actin depolymerization protein that promotes filament fragmentation, was also investigated. Immunofluorescence data showed that all of these proteins were present around rGO contact sites (Figure 7B and Figure S12-13) and that their protein levels were all altered after rGO treatment in cortical neurons and PC12 cells. Over time, the expression levels of cortactin and cofilin first increased and then decreased, whereas those of ARP2 and ARP3 proteins showed sustained increases until 24 h (Figure S12C and S14). These data indicated that actin dynamic-related proteins had been activated and effectively recruited around the contact sites with rGO.

We then investigated whether these recruited proteins contributed to the generation of actin dots. The ARP2/ARP3 complex and cortactin can function only when they form an actin nucleation complex, which is the key machinery for actin polymerization at the plus end. Our Co-IP results showed that the combination of cortactin, ARP2/ARP3 and β-actin was markedly decreased after rGO exposure for 6 h, indicating that the formation of the actin nucleation complex had been blocked, which led to the interruption of actin polymerization (Figure 7C). We then evaluated the entire actin assembly and disassembly status by detecting the relative levels of assembled actin (F-actin) and actin monomers (G-actin). Additionally, some actin-binding compounds, including jasplakinolide (Jasp), a structurally related prototypic actin stabilizer that acts by blocking the minus end of actin, and cytochalasin D (Cyto D), an actin polymerization inhibitor that acts by capping the plus end of actin, were used. Slight actin disassembly was observed starting after 1 h of

exposure to rGO, and Jasp and Cyto D significantly induced actin assembly and disassembly, respectively. Extension of the treatment time to 12 h induced more extensive actin disassembly (Figure 7D). Based on the above findings, it is reasonable to speculate that although ARP2/ARP3 and cortactin were recruited to the area surrounding the rGO contact sites, they were unable to form actin nucleation complexes to repair the disassembled actin system, and the actin disassembly evolved into the main actin status.

Most importantly, Jasp and NAC both exert protective effects on actin dynamics. The generation of actin dots around the rGO materials was inhibited to some extent after the addition of Jasp and NAC (Figure S15). Moreover, NAC treatment also largely prevented the recruitment of actin polymerization-related proteins and recovered the formation of actin nucleation complex (Figure 7B-D and Figure S12). The reason for these findings probably involves the fact that the oxidized rGO possessed a high number of oxygen-containing groups: upon their fusion with and penetration of the plasma membrane, the oxidized flakes induced a local highly oxidizing environment, similar to that created by GO.[18,19] The local highly oxidizing environment subsequently blocked the formation of actin nucleation complexes.

**Actin Disturbance Involves in the rGO-Induced Neurotransmission Depression.**

The controlled release and recycling of neurotransmitters require balanced actin dynamics due to their essential roles in regulating pre- and postsynaptic physiology.[35,38,39] Our electrophysiological data showed that oxidized rGO can depress the neurotransmission process, as evidenced by mEPSC alterations. Importantly, oxidized rGO not only

penetrated the cell membrane but also gradually disturbed the actin dynamics. Thus, whether actin disturbance was the key factor in the inhibitory effects on the neurotransmission process was investigated.

First, we determined the neuronal release capacity of glutamate, which is the main excitatory neurotransmitter in the mammalian central nervous system and mediates neuronal development, migration, synaptic maintenance and transmission. After glutamate pretreatment, higher intracellular glutamate levels were detected in the rGO-treated group than in the control group, which suggested that rGO had potent inhibitory effects on the neuronal release capacity. This inhibitory effect was significantly reversed by NAC (Figure 8A). Furthermore, to ascertain whether the rGO-mediated interference of synaptic activity affected the synaptic exocytosis process, leading to decreased neurotransmitter release, we measured the exocytosis kinetics of synaptic vesicles by real-time imaging of FM dye destaining (Figure 8B).[40] After the FM dye was loaded into all releasable synaptic vesicle pools, the neurons were treated with or without rGO for 3 h, and the rate of presynaptic vesicle exocytosis was then monitored under high potassium activation. We found that prior to high potassium activation, the fluorescence intensity of the synaptic terminals showed no pronounced changes in either the control or rGO treatment groups (data not shown). However, after high potassium induced maximum exocytosis, the rGO treatment group exhibited a notably lower release rate than the control group. Additionally, the clusters of presynaptic terminals in the rGO treatment group manifested as bright fluorescent spots that remained visible after 1 min of destaining, whereas in the control

group, the spots became dim. These results indicated that rGO treatment potently blocked the synaptic exocytosis process.

To verify the mechanism underlying the abnormal exocytosis process of synaptic vesicles, we detected synaptic vesicle fusion-related proteins (also called SNARE proteins), including Syt1, synaptic vesicle-associated membrane protein 2 (VAMP2), and VAMP7. These proteins, which are involved in the docking and fusion of synaptic vesicles, are the master mediators that allow neurons to release neurotransmitters.[41] Therefore, the abnormal translocation of SNARE proteins to the plasma membrane in neurons was analyzed to reveal the blockage effects on cellular exocytosis. We used this approach because it would have been difficult to detect the status of the subcellular compartments and proteins in synapses using biochemical detection methods. Our data showed potent time-dependent increases in the levels of these SNARE proteins in cortical neurons after rGO treatment (Figure S16). However, the membrane levels of these proteins after 12 h of rGO treatment were lower than those in the control group, and NAC significantly reversed this inhibitory effect (Figure 8C). These data demonstrated that the exocytosis-related proteins had difficultly translocating onto the cell membrane, which suggested that the docking and fusion processes of the synaptic vesicles had been blocked after rGO treatment. The increases in the expression levels of these exocytosis-related proteins were likely a feedback response caused by abnormal exocytosis.

To determine whether the oxidized rGO-induced actin disturbance was the main cause of the inhibition of synaptic vesicle docking and fusion, we used Cyto D as a positive

control for the depolymerization of actin filaments. Intriguingly, Cyto D decreased the protein levels of Syt1, VAMP2 and VAMP7 on the cell membrane, which was similar to the effect of rGO. Jasp showed no effects on these protein levels on the cell membrane but significantly reversed the rGO-induced decrease in the membrane protein levels of these SNARE proteins to some extent (Figure 8D). In addition, we detected the distribution of Syt1-containing vesicles *via* GFP-Syt1 plasmid transfection and found fewer Syt1-containing vesicles on the actin-linked cell membrane in the rGO-treated group than in the control group. Similar results were also observed for Cyto D. Most importantly, more Syt1-containing vesicles were located on the cell membrane after rGO treatment in the presence of Jasp than after rGO treatment alone (Figure 8E). These data indicated that the rGO-induced actin disturbance likely blocked the docking and fusion process of synaptic vesicles and that Jasp markedly reversed this phenomenon by promoting actin polymerization.

To verify this conclusion, the patch clamp technique was used to detect mEPSCs. As we observed previously, rGO significantly decreased the frequency and amplitude of mEPSCs and increased their rise time without affecting their decay time. Importantly, the rGO-induced decreases in the frequency and amplitude of mEPSCs were largely reversed in the presence of Jasp, signifying that the extent of synaptic vesicles exocytosis increased. The rise time of mEPSCs was also increased, which indicated that exocytosis occurred more rapidly (Figure 8F).

Actin stability is a dynamic process consisting of actin assembly at the plus end and

actin disassembly at the minus end. All changes in actin induced by Jasp or Cyto D, regardless of the plus or minus end of actin, could affect the neurotransmission process.[39,42,43] In this study, both the plus and minus ends were the main targets of rGO that induced actin disturbance. The plus end was capped due to inhibition of actin nucleation complex formation, and the minus end was accelerated due to the increased cofilin protein levels. Jasp is an actin stabilizer that acts by blocking the minus end of actin and might not affect the inhibitory effects on the plus end, which limits its protective effects on actin dynamics and neurotransmission.

With the exception of the rGO-targeted actin system in this study, many physicochemical properties of GFNs exert various effects on neurotransmission. The high edge/defect levels and fewer layer numbers would affect neurotransmission due to an increased surface area, and active sites can adsorb many more biological molecules and active species on the lattice surface for reaction. Furthermore, some metal ions, such as $Ca^{2+}$, $Mn^{2+}$, $Na^{+}$, and $Fe^{2+}$, are the main impurities generated during GFNs and other carbon-based nanomaterials synthesis, and these ions also reportedly induce some effects on neurological function.[44,45] For example, $Mn^{2+}$ can potently cause aberrant glutamate replenishment/transport, leading to disturbance of glutamate metabolism and consequently neurotransmission disruption.[46] Intriguingly, the presence of metallic impurities can alter and even regulate the electrochemical and oxidation properties of GFNs, which exerts positive effect in neurology and promote the scope and effectiveness of GFNs' neural applications.[47,48]

In this study, defects on the rGO surface and edges were characterized and manifested by the presence of the D peak in Raman spectrum, and these defects were the basis for biological oxidation due to the active sites they provide. However, the impurities might not be an influential factor due to the high purity of the rGO material we used, as detected *via* ICP-MS (Table S1). We further collected intracellular rGO (located in the cytoplasm and plasma membrane) and extracellular rGO. AFM results showed that the thickness of extracellular rGO (almost 3-4 nm, indicating four to six layers of rGO) was markedly higher than that of intracellular rGO (almost 800 pm-1 nm, indicating single-layer rGO) (Figure S17A-C). Considering the face-to-face stacked effects of GFNs,[49,50] rGO shows agglomeration in culture environments and the stacked nanosheets have more difficulty in contacting and piercing into the plasma membrane due to their higher thickness, whereas the single-layer nanosheets are more easily fused with the cell membrane and endocytosed.[51] Most importantly, as Raman spectrum data showed, the single-layer nanosheets exhibited higher defect sites for oxidation,[52,53] which directly enhanced their uptake efficiency (Figure S17D).

**Conclusion**

In this study, we revealed that the cellular oxidation process of rGO in neuronal cells occurred without the addition of foreign oxidants. The activation of cellular redox signaling, which involves NOXs and mitochondria, significantly increased the cellular ROS level and intensified the oxidation of rGO. Importantly, oxidized rGO showed a higher affinity for the cell membrane and induced membrane perturbance, ultimately leading to the

depression of neurotransmission. The remolding of actin filaments was proven to be the main mechanism through which oxidized rGO modulated neurotransmission. Taken together, our investigation of the mechanism suggests that rGO could be exploited as a neurotransmission modulator and that the corresponding effects can be controlled by regulating the cellular oxidation process and thus the actin dynamics. Our study improves the understanding of the potential applications of GFNs in neurology and provides useful information for the design of GFN-based materials.

## Tables

**Table 1 Characteristic of rGO**

| | DLS | | Zeta potential | Raman spectrum |
|---|---|---|---|---|
| | Water | Culture medium | | |
| rGO | 98.4 ± 21.3 nm | 189.9 ± 31.1 nm | -12.5 ± 4.7 mV | D peak: 1347.6 $cm^{-1}$<br>G peak: 1585.5 $cm^{-1}$<br>G' peak: 2703.4 $cm^{-1}$ |

**Table 2 Atomic % concentration of oxidized groups on rGO surface by XPS**

| | rGO | rGO exposed to cells for 30 min | rGO exposed to cells for 1 h | rGO exposed to cells for 3 h | rGO+NAC exposed to cells for 3 h | rGO exposed to extracellular environment for 3 h |
|---|---|---|---|---|---|---|
| C=O | 4.24 | 4.23 | 4.04 | 4.21 | 4.38 | 4.43 |
| C–O–C | 5.32 | 5.44 | 5.45 | 5.54 | 5.90 | 5.70 |
| C–OH | 1.84 | 5.74 | 7.63 | 9.41 | 3.17 | 2.52 |
| Total oxygen | 11.40 | 15.41 | 17.12 | 19.16 | 13.45 | 12.65 |
| C/O ratio | 7.77 | 5.49 | 4.84 | 4.22 | 6.43 | 6.91 |

## Materials and Methods

**Chemicals.** Phalloidin-iFluor 594, Jasp and anti-NSE, -cortactin were purchased from Abcam (USA). Cyto D was purchased from Aladdin (China). NAC was purchased from Sigma-Aldrich (USA). Apo, GKT, ML171 were purchased from Selleck (USA) and mTP was from APExBIO (USA). Anti-ARP3, -ARP2, -cofilin1, -Rac1, -Rac2, and -p67$^{phox}$ were purchased from Proteintech (USA). Anti-p-p47$^{phox}$ and -p-p67$^{phox}$ were purchased from Affinity (USA). Anti-NOX1, -NOX2, -NOX4, and -NOXA1 were purchased from ABclonal (USA) and Anti-NOXO1 was from geneTEX (USA).

**Preparation of rGO.** The preparation of rGO was carried out using Vitamin C.[54] In detailed, 100 mg Vitamin C were added into 100 mL GO nanosheet (0.1 mg/mL, Nanoinnova, Spain) well-dispersed suspension. The reduction process was undergoing at 95℃ for 12 h. After removing residual impurities in deionized water by rinsing, the materials were collected *via* vacuum-drying at 60℃ for 3 h. The rGO materials used in this study was obtained.

**Characterization of rGO.** The surface topography of rGO was analyzed using an AFM instrument (MFP-3D-S, Asylum Research, USA) equipped with a silicon nitride probe. Images were taken using tapping-mode in air by depositing 20 $\mu$L of 100 $\mu$g/mL rGO on a freshly cleaved mica surface (Agar Scientific, UK) coated with poly-L-lysine 0.01% (Sigma-Aldrich, USA) and dried in air. Images were taken at random locations in the sample under ambient conditions with a scanning rate of 1 Hz and a scanning angle of 90°. Raman spectroscopy (Dimension Edge, Bruker, Germany) was used to measure the

structural features of rGO. The measurements were performed using a 100× objective with a laser excitation (50 mW, Torus) of 532 nm. The zeta potential and hydrodynamic diameter of rGO (10 $\mu$g/mL) in deionized water and culture medium were detected using a Zetasizer (Malvern Zetasizer Nano, Malvern Panalytical, UK). XRD was performed using an X-ray diffractometer (D8 ADVANCE, Bruker, Germany), at 40 kV and 15 mA in the range of $2\theta$ = 5-60° with a scanning rate of 10 degree/min and CuKα radiation (λ = 1.540 Å). XPS (K-Alpha, Thermo Fisher, USA) with a monochromatic Al Kα source of 1486.68 eV (aluminum anode) and 15 kV was used to investigate the chemical state and the oxidized groups on the rGO surface. After charge correction, data analyses and curve fitting were performed using Gaussian components with CasaXPS program (Casa Software, UK) after Shirley background subtraction. rGO samples for elemental analysis were prepared in deionized water, and the concentrations of metals and metalloids contained in the samples were determined using an Agilent model 7500 ICP-MS (USA).

**Cell Culture.** The PC12 cell line was cultured in DMEM containing 10% FBS (Thermo Fisher, USA). Dissociated cortical neurons were prepared from wild-type Sprague-Dawley rats as previously described,[8] and the experimental protocol was approved by the Southern Medical University Ethics and Experimentation of Committee (No. L2017189). Briefly, 18-day-old embryos were removed immediately by cesarean section, and the enzymatically dissociated cortical neurons were plated on poly-D-lysine-coated (0.1 mg/mL, Solarbio, China) glass coverslips and cultured in Neurobasal medium containing B27 supplement (Thermo Fisher, USA). The neurons were used for experiments after 14 days of culture.

**Isolation and Detection of Oxidized rGO.** Cells were treated with 20 $\mu$g/mL rGO or cell culture supernatants. At the end of treatment, cells were washed to remove the unattached rGO and were then lysed. For the isolation of oxidized rGO, collected materials were washed with hydrochloric acid and ethanol repeatedly to remove the salts and organic components from the cells and culture supernatants, as previously described.[14] The materials obtained from cells were collected by centrifugation and freeze-drying.

**ESR Measurements.** ESR spectroscopy (Bruker, Germany) is a sensitive and specific technique for studying the radicals formed in chemical reactions and 5,5-dimethyl-1-pyrroline N-oxide (DMPO, Sigma-Aldrich, USA) was employed to stabilize •OH species.[55] Reactions were initiated by adding 1 mM $H_2O_2$ and ESR spectra for all sample solutions were recorded 1.5 min after mixing. 4 lines occurred in the presence of rGO, DMPO and $H_2O_2$ is assigned to spin adduct DMPO/•OH.

**DFT Calculation.** To properly describe the solid-liquid interface, DFT calculations with implicit CANDLE solvation model were performed using JDFTx 1.5.0.[56,57] The Perdew-Burke-Ernzerhof (PBE) functional[58] and GBRV ultrasoft pseudopotentials (USPP)[59] were used, with a plane wave cutoff of 544 eV (20 a.u.). Single gamma-point sampling was used for Brillouin zone integration. The geometry optimization and self-consistent field convergence criteria were set to 0.02 eV/Å and $10^{-6}$ eV, respectively.

**Electron Microscopy Analysis.** First, after PC12 cells or cortical neurons were treated with rGO for 1 h, the cells were fixed with 2.5% glutaraldehyde and dehydrated using graded ethanol. The interactions between rGO nanosheets and the plasma membrane were

detected using SEM (SU3800, HITACHI, Japan). Second, after the cells were incubated with rGO for 30 min or 6 h, the endocytosis of rGO and the mitochondrial structure were observed *via* TEM. Cells were collected by scraping, fixed with 2.5% glutaraldehyde, dehydrated through a series of graded ethanol solutions followed by acetone, and then embedded. Ultrathin sections were prepared for observation using a Hitachi H-7500 TEM (Hitachi, Japan).

**Detection of Membrane Lipid Peroxidation.** The cells were incubated with 10 $\mu$M BODIPY 581/591 C11 peroxidation probe (Thermo Fisher, USA) for 30 min. Cellular fluorescence of the reduced and oxidized fluorescent dye at excitation/emission wavelengths of 581/591 nm (Texas Red filter set) and 488/510 nm (traditional FITC filter), respectively, was observed *via* a FV10i confocal microscope (Olympus, Japan). FITC fluorescence was analyzed using Image-Pro Plus 6.0 software.

**Detection of Cellular ROS and mtROS.** The cells were incubated with 10 $\mu$M DCFH-DA for 30 min for cellular ROS detection or incubated with 5 $\mu$M MitoSOX™ Red indicator (Thermo Fisher, USA) for 30 min for mtROS level detection. The measurements were conducted using a BMG microplate reader (SPECTROstar Omega, Germany).

**Flow Cytometry Analysis.** After PC12 cells and cortical neurons were treated with rGO (20 $\mu$g/mL) in the presence or absence of NAC, SSCs and FSCs were analyzed immediately by flow cytometry (BD FACSAria III; BD, USA).

**Patch Clamp Electrophysiological Recording.** Cultured cortical neurons were exposed to 20 $\mu$g/mL rGO or GO nanosheets, and whole-cell recordings were obtained at room

temperature with pipettes (5-7 MΩ) containing the following (in mM): 120 K gluconate, 20 KCl, 10 HEPES, 10 EGTA, 2 $MgCl_2$, and 2 $Na_2ATP$ at pH 7.3 and an osmolarity of 300 mOsm. The extracellular solution contained the following (in mM): 150 NaCl, 4 KCl, 1 $MgCl_2$, 2 $CaCl_2$, 1 $MgCl_2$, 10 HEPES, and 10 glucose at pH 7.4. TTX (1 $\mu$M) was used to block the generation and propagation of spontaneous action potentials. Data were collected by a Multiclamp 700B patch amplifier (Axon CNS, Molecular Devices, USA) and digitized at 10 kHz with pClamp 10.2 acquisition software (Molecular Devices, USA). Spontaneous synaptic activity was recorded by clamping the membrane voltage at a -56 mV holding potential. All recorded events were analyzed offline with AxoGraph 1.4.4 (Axon Instrument) event detection software (Axon CNS, Molecular Devices, USA).

**Plasmid and siRNA Construction and Transfection.** The siRNA (siNOX1 and siNOX2) and plasmid constructs (GFP-Syt1) were obtained from Ribobio (China) and Vigenebio (USA) respectively, and transfection was carried out in Opti-MEM medium using Lipofectamine 2000 (Invitrogen, Thermo Fisher, USA) according to the manufacturer's protocol.

**Western Blot Analysis.** Cells were collected and lysed with RIPA (Beyotime, China) containing protease and phosphatase inhibitor cocktail (MCE, USA). Equal amounts of protein were added and separated by 10% SDS-PAGE. The proteins were transferred and then blocked. After incubation overnight with primary antibodies at 4°C and the corresponding secondary antibody, detection was carried out using an ECL kit (WBLKS0500, Merck Millipore, USA) and Tanon 5200 automatic chemiluminescence

image analysis system (China).

**Co-IP Analysis.** Cells were lysed with binding buffer (50 mM Tris, 150 mM NaCl, and 0.1% TritonX-100, pH 7.5) containing protease inhibitor cocktail on ice. Both magnetic beads and primary antibody were incubated in the cell lysate overnight at 4°C. The beads were magnetically separated and washed with wash buffer (50 mM Tris, 150 mM NaCl, and 0.1% TritonX-100, pH 7.5). Loading buffer (2×) was added to the antigen-antibody-bead complex and heated at 95°C for 10 min, and then the beads were separated by centrifugation. The antigen-antibody complex was collected for western blot analysis, and the whole-cell lysates were blotted and shown as input groups.

**Immunofluorescence Staining.** Cells were fixed with 4% paraformaldehyde for 20 min and permeabilized with 0.5% Triton X-100 for 10 min. After blocking with 5% FBS for 1 h, the cells were incubated with primary antibodies overnight at 4°C and then with the corresponding second antibody for 1 h at 37°C. Cellular fluorescence was observed *via* an FV10i confocal microscope.

**Isolation of Plasma Membrane Protein.** The Minute™ Plasma Membrane Protein Isolation and Cell Fractionation Kit (Invent, USA) was used according to the manufacturer's instructions. Briefly, cells were treated with buffer A and then transferred to the filter cartridges for differential centrifugation and density centrifugation to separate the membrane protein and other cell components. Total membrane protein was collected after suspension in buffer B and centrifugation. Minute™ denaturing protein solubilization reagent was used to dissolve the isolated plasma membrane proteins before western blot

analysis.

**Detection of MMP.** Cells were stained with 200 nM TMRE (Thermo Fisher, USA) for 30 min at 37℃. Cellular fluorescence was observed with FV10i confocal microscope (Olympus, Japan) after coincubation with MitoTracker (100 nM, Thermo Fisher, USA). The fluorescence intensities of TMRE were also analyzed by flow cytometry.

**Detection of ATP Content.** An ATP assay kit (Beyotime, China) was used to estimate the intracellular level of ATP. Ccells were lysed on ice and centrifuged at 12000 g for 5 min. The supernatants were collected and incubated with ATP working solution. Fluorescence was measured by a BMG microplate reader.

**Detection of ETC Complex Activity.** The enzymatic activities of ETC I-V were measured using commercially available kits (Solarbio, China) according to the manufacturer's instructions. PC12 cells were lysed on ice and incubated with working solution accordingly. Complex I activity was measured as the rotenone-sensitive decrease in the absorbance of NADH at 340 nm. Complex II activity was measured as the rate of 2,6-dichlorophenol indophenol reduction, which corresponded to a decrease in absorbance at 600 nm. Complex III activity was measured as the generation of reduced cytochrome C at 550 nm. Complex Ⅳ activity was measured as the rate of reduced cytochrome C reduction, which corresponded to a decrease in absorbance at 550 nm. Complex V activity was measured as the rate of Pi generation, which corresponded to an increase in absorbance at 660 nm.

**Cell Fluorescence Imaging of Actin Filaments.** After PC12 cells and cortical neurons were treated with rGO, the cells were gently washed with PBS, fixed with 4%

paraformaldehyde and incubated with phalloidin-iFluor 594 for 1 h. Images were obtained using an FV10i confocal microscope.

**Isolation of Polymerized and Depolymerized Actin Filaments.** The F/G-actin ratio were measured as previously described.[60] Cortical neurons were lysed with actin stabilization buffer (0.1 M PIPES, 30% glycerol, 5% DMSO, 1 mM $MgSO_4$, 1 mM EGTA, 1% TritonX-100, 1 mM ATP, and protease inhibitor, pH 6.9) on ice and centrifuged at 16000 g for 75 min. The supernatant containing G-actin was transferred to another tube, and the pellet containing F-actin was dissolved in actin depolymerization buffer (0.1 M PIPES, 1 mM $MgSO_4$, 10 mM $CaCl_2$, and 5 $\mu$M Cyto D, pH 6.9). Aliquots of the supernatant and pellet fractions were separated on 10% SDS-PAGE gels and then western blotted with monoclonal anti-β-actin.

**Detection of Neurotransmitter Release Capacity.** Neurons were washed with warm PBS and incubated with 100 $\mu$M glutamate (Sigma-Aldrich, USA) in the culture medium for 1 h. After wiping off the unabsorbed glutamate, the neurons were exposed to rGO for various durations. The intracellular concentration of glutamate was detected using a commercial kit (Solarbio, China) according to the manufacturer's instructions.

**Detection of FM Dye.** The cationic styrylpyridinium dye FM 1-43 (Invitrogen, Thermo Fisher, USA) was utilized for the detection of synaptic vesicle kinetics.[40] Briefly, the cells were incubated for 10 min in a Tyrode's solution, and then incubated for 2 min with FM1-43 dye (10 $\mu$M) in high-potassium (50 mM) buffer. After treatment with rGO containing FM1-43 dye (2.5 $\mu$M) for 3 h, the cells were washed for 10 min with a calcium-free low-

potassium Tyrode's buffer to remove the surface-bound dye using ADVASEP-7 (Biotium, USA), and baseline measurements were then acquired over 30 s. Subsequently, the cells were stimulated for 3 min with high potassium medium to induce dye destaining. Images were acquired using an FV10i confocal microscope. For the analysis of FM1-43, different fields were selected randomly and individual synapses were analyzed. To determine the extent of dye release, the values were normalized to the initial fluorescence (F/F0). When the rate of dye release was calculated, the fluorescence remaining in each synapse at the end of the stimulation period was subtracted from all the values and then normalized to the initial fluorescence.

**Statistical Analysis.** At least three independent assays were performed for each experiment. Data were analyzed by analysis of variance followed by the Bonferroni post hoc test, and the results are represented as the mean ± SD. A *p*-value less than 0.05 was considered significant.

**Acknowledgements**

The authors declare no competing financial interest. This Project is funded by the National Key Research and Development Program of China (2016YFC1102605, 2016YFC1102603), the National Natural Science Foundation of China (81870786), the Natural Science Foundation of Guangdong Province (2018030310291, 2019A1515011980).

**Supporting Information**

The Supporting Information is available free of charge on the ACS Publications website at http://pubs.acs.org.

Detailed information including: the experimental method for elemental analysis and AFM characterization of rGO materials and cell viability tests. Supplementary figures showing the characterization and neurotransmission modulatory effects of GO; XPS survey of rGO; cell identifications, cellular viability and uptake efficiency after rGO treatment; DFT calculation of the density of state; XPS of rGO reacting with $H_2O_2$; different cellular reaction induced by *c*-rGO and *p*-rGO; NOX2 activation in PC12 cells; blockage of NOX2 activation and rGO oxidation in PC12 cells by siRNA; blockage of neuronal NOX1 activation by siRNA and NOX inhibitors; MMP detection in PC12 cells; actin dynamic alterations in PC12 cells and cortical neurons; detection of synaptic vesicle-related protein expression in neurons; and AFM and Raman spectroscopy characterizing extracellular and intracellular rGO.

## References


1. Loh, K. P.; Ho, D.; Chiu, G. N. C.; Leong, D. T.; Pastorin, G.; Chow, E. K. Clinical Applications of Carbon Nanomaterials in Diagnostics and Therapy. *Adv Mater* **2018**, *30*, e1802368.
2. Pampaloni, N. P.; Lottner, M.; Giugliano, M.; Matruglio, A.; D'Amico, F.; Prato, M.; Garrido, J. A.; Ballerini, L.; Scaini, D. Single-Layer Graphene Modulates Neuronal Communication and Augments Membrane Ion Currents. *Nat Nanotechnol* **2018**, *13*, 755-764.
3. Wan, C. J.; Liu, Y. H.; Feng, P.; Wang, W.; Zhu, L. Q.; Liu, Z. P.; Shi, Y.; Wan, Q. Flexible Metal Oxide/Graphene Oxide Hybrid Neuromorphic Transistors on Flexible Conducting Graphene Substrates. *Adv Mater* **2016**, *28*, 5878-5885.
4. Wang, K.; Frewin, C. L.; Esrafilzadeh, D.; Yu, C.; Wang, C.; Pancrazio, J. J.; Romero-Ortega, M.; Jalili, R.; Wallace, G. High-Performance Graphene-Fiber-Based Neural Recording Microelectrodes. *Adv Mater* **2019**, *31*, e1805867.
5. Rauti, R.; Medelin, M.; Newman, L.; Vranic, S.; Reina, G.; Bianco, A.; Prato, M.; Kostarelos, K.; Ballerini, L. Graphene Oxide Flakes Tune Excitatory Neurotransmission *In Vivo* by Targeting Hippocampal Synapses. *Nano Lett* **2019**, *19*, 2858-2870.
6. Rauti, R.; Lozano, N.; León, V.; Scaini, D.; Musto, M.; Rago, I.; Ulloa Severino, F. P.; Fabbro, A.; Casalis, L.; Vázquez, E.; Kostarelos, K.; Prato, M.; Ballerini, L. Graphene Oxide Nanosheets Reshape Synaptic Function in Cultured Brain Networks. *ACS Nano* **2016**, *10*, 4459-4471.
7. Yinfeng, L.; Hongyan, Y.; Annette, V. D. B.; Megan, C.; Hurt, R. H.; Kane, A. B.; Huajian, G. Graphene Microsheets Enter Cells through Spontaneous Membrane Penetration at Edge Asperities and Corner Sites. *Proc Natl Acad Sci U S A* **2013**, *110*, 12295-12300.
8. Bramini, M.; Sacchetti, S.; Armirotti, A.; Rocchi, A.; Vazquez, E.; Leon Castellanos, V.; Bandiera, T.; Cesca, F.; Benfenati, F. Graphene Oxide Nanosheets Disrupt Lipid Composition, Ca(2+) Homeostasis, and Synaptic Transmission in Primary Cortical Neurons. *ACS Nano* **2016**, *10*, 7154-7171.
9. Ou, L.; Song, B.; Liang, H.; Liu, J.; Feng, X.; Deng, B.; Sun, T.; Shao, L. Toxicity of Graphene-Family Nanoparticles: A General Review of the Origins and Mechanisms. *Part Fibre Toxicol* **2016**,

*13*, 57.

10. Kang, Y.; Liu, J.; Wu, J.; Yin, Q.; Liang, H.; Chen, A.; Shao, L. Graphene Oxide and Reduced Graphene Oxide Induced Neural Pheochromocytoma-Derived PC12 Cell Lines Apoptosis and Cell Cycle Alterations *via* the ERK Signaling Pathways. *Int J Nanomedicine* **2017**, *12*, 5501-5510.
11. Xiao, H.; Xiaoying, Q.; Freddy, B.; Hua, Z. Graphene-Based Composites. *Chem Soc Rev* **2012**, *41*, 666-686.
12. Hada, M.; Miyata, K.; Ohmura, S.; Arashida, Y.; Ichiyanagi, K.; Katayama, I.; Suzuki, T.; Chen, W.; Mizote, S.; Sawa, T.; Yokoya, T.; Seki, T.; Matsuo, J.; Tokunaga, T.; Itoh, C.; Tsuruta, K.; Fukaya, R.; Nozawa, S.; Adachi, S.-i.; Takeda, J.; *et al*. Selective Reduction Mechanism of Graphene Oxide Driven by the Photon Mode *versus* the Thermal Mode. *ACS Nano* **2019,** *13* 10103-10112.
13. Liu, L.; Zhu, C.; Fan, M.; Chen, C.; Huang, Y.; Hao, Q.; Yang, J.; Wang, H.; Sun, D. Oxidation and Degradation of Graphitic Materials by Naphthalene-Degrading Bacteria. *Nanoscale* **2015**, *7*, 13619-13628.
14. Guo, Z.; Xie, C.; Zhang, P.; Zhang, J.; Wang, G.; He, X.; Ma, Y.; Zhao, B.; Zhang, Z. Toxicity and Transformation of Graphene Oxide and Reduced Graphene Oxide in Bacteria Biofilm. *Sci Total Environ* **2017**, *580*, 1300-1308.
15. Ambrosi, A.; Chua, C. K.; Khezri, B.; Sofer, Z.; Webster, R. D.; Pumera, M. Chemically Reduced Graphene Contains Inherent Metallic Impurities Present in Parent Natural and Synthetic Graphite. *Proc Natl Acad Sci U S A* **2012**, *109*, 12899-12904.
16. Wong, C. H. A.; Sofer, Z.; Kubešová, M.; Kučera, J.; Matějková, S.; Pumera, M. Synthetic Routes Contaminate Graphene Materials with a Whole Spectrum of Unanticipated Metallic Elements. *Proc Natl Acad Sci U S A* **2014**, *111*, 13774-13779.
17. Krishnamoorthy, K.; Veerapandian, M.; Yun, K.; Kim, S.-J., The Chemical and Structural Analysis of Graphene Oxide with Different Degrees of Oxidation. *Carbon* **2013**, *53*, 38-49.
18. Li, R.; Mansukhani, N. D.; Guiney, L. M.; Ji, Z.; Zhao, Y.; Chang, C. H.; French, C. T.; Miller, J. F.; Hersam, M. C.; Nel, A. E.; Xia, T. Identification and Optimization of Carbon Radicals on

Hydrated Graphene Oxide for Ubiquitous Antibacterial Coatings. *ACS Nano* **2016**, *10*, 10966-10980.

19. Li, R.; Guiney, L. M.; Chang, C. H.; Mansukhani, N. D.; Ji, Z.; Wang, X.; Liao, Y. P.; Jiang, W.; Sun, B.; Hersam, M. C.; Nel, A. E.; Xia, T. Surface Oxidation of Graphene Oxide Determines Membrane Damage, Lipid Peroxidation, and Cytotoxicity in Macrophages in a Pulmonary Toxicity Model. *ACS Nano* **2018,** *12*, 1390-1402.
20. Yang, Z.; Jin, J.; Yuan, G.; Jun, M.; Su-Yan, P.; Juan, L.; Xue-Ting, L.; Li-Peng, Y. Activation of Peroxymonosulfate by Benzoquinone: A Novel Nonradical Oxidation Process. *Environ Sci Technol* **2015**, *49*, 12941-12950.
21. Duan, X.; Ao, Z.; Sun, H.; Indrawirawan, S.; Wang, Y.; Kang, J.; Liang, F.; Zhu, J.; Wang, S. Nitrogen-Doped Graphene for Generation and Evolution of Reactive Radicals by Metal-Free Catalysis. *ACS Appl Mater Interfaces* **2015**, *7*, 4169-4178.
22. Sun, H.; Liu, S. Z.; Zhou, G.; Ang, M.; Tade, M.; Wang, S. Reduced Graphene Oxide for Catalytic Oxidation of Aqueous Organic Pollutants. *ACS Appl Mater Interfaces* **2012**, *4*, 5466-5471.
23. Wang, L.; Hu, C.; Shao, L. The Antimicrobial Activity of Nanoparticles: Present Situation and Prospects for the Future. *Int J Nanomedicine* **2017**, *12*, 1227-1249.
24. Tejero, J.; Shiva, S.; Gladwin, M. T. Sources of Vascular Nitric Oxide and Reactive Oxygen Species and Their Regulation. *Physiol Rev* **2019**, *99*, 311-379.
25. Fan, X.; Zhang, G.; Zhang, F. Multiple Roles of Graphene in Heterogeneous Catalysis. *Chem Soc Rev* **2015**, *44*, 3023-3035.
26. Song, Y.; Qu, K.; Zhao, C.; Ren, J.; Qu, X. Graphene Oxide: Intrinsic Peroxidase Catalytic Activity and Its Application to Glucose Detection. *Adv Mater* **2010**, *22*, 2206-2210.
27. Mao, J.; Guo, R.; Yan, L. T. Simulation and Analysis of Cellular Internalization Pathways and Membrane Perturbation for Graphene Nanosheets. *Biomaterials* **2014**, *35*, 6069-6077.
28. Bramini, M.; Chiacchiaretta, M.; Armirotti, A.; Rocchi, A.; Kale, D. D.; Martin, C.; Vázquez, E.; Bandiera, T.; Ferroni, S.; Cesca, F.; Benfenati, F. An Increase in Membrane Cholesterol by Graphene Oxide Disrupts Calcium Homeostasis in Primary Astrocytes. *Small* **2019**, *15*, 1900147.

29. Abhilash, S.; Panchakarla, L. S.; Parwathy, C.; Deepthy, M.; Shantikumar, N.; Rao, C. N. R.; Manzoor, K. Differential Nano-Bio Interactions and Toxicity Effects of Pristine *versus* Functionalized Graphene. *Nanoscale* **2011**, *3*, 2461-2464.

30. Marone, I. M.; De Logu, F.; Nassini, R.; Muryel, D. C. G.; Benemei, S.; Ferreira, J.; Jain, P.; Puma, S. L.; Bunnett, N. W.; Geppetti, P., Materazzi, S. TRPA1/NOX in the Soma of Trigeminal Ganglion Neurons Mediates Migraine-Related Pain of Glyceryl Trinitrate in Mice. *Brain* **2018**, *141*, 2312-2328.

31. Ma, M. W.; Jing, W.; Dhandapani, K. M.; Wang, R.; Brann, D. W. NADPH Oxidases in Traumatic Brain Injury – Promising Therapeutic Targets? *Redox Biol* **2018**, *16*, 285-293.

32. Shadel, G. S.; Horvath, T. L. Mitochondrial ROS Signaling in Organismal Homeostasis. *Cell* **2015**, *163*, 560-569.

33. Sies, H.; Berndt, C.; Jones, D. P. Oxidative Stress. *Annu Rev Biochem* **2017**, *86*, 715-748.

34. Zorov, D. B.; Juhaszova, M.; Sollott, S. J. Mitochondrial Reactive Oxygen Species (ROS) and ROS-Induced ROS Release. *Physiol Rev* **2014**, *94*, 909-950.

35. Li, P.; Bademosi, A. T.; Luo, J.; Meunier, F. A. Actin Remodeling in Regulated Exocytosis: Toward a Mesoscopic View. *Trends Cell Biol* **2018**, *28*, 685-697.

36. Sakai, J.; Li, J.; Subramanian, K. K.; Mondal, S.; Bajrami, B.; Hattori, H.; Jia, Y.; Dickinson, B. C.; Zhong, J.; Ye, K., Chang, C. J.; Ho, Y. S.; Zhou, J.; Luo, H. R. Reactive Oxygen Species-Induced Actin Glutathionylation Controls Actin Dynamics in Neutrophils. *Immunity* **2012**, *37*, 1037-1049.

37. Liu, J.; Kang, Y.; Yin, S.; Chen, A.; Wu, J.; Liang, H.; Shao, L. Key Role of Microtubule and Its Acetylation in a Zinc Oxide Nanoparticle-Mediated Lysosome-Autophagy System. *Small* **2019**, *15*, e1901073.

38. Leterrier, C.; Dubey, P.; Roy, S. The Nano-Architecture of the Axonal Cytoskeleton. *Nat Rev Neurosci* **2017**, *18*, 713-726.

39. Cingolani, L. A.; Goda, Y., Actin in Action: The Interplay between the Actin Cytoskeleton and Synaptic Efficacy. *Nat Rev Neurosci* **2008**, *9*, 344-356.

40. Collado-Alsina, A.; Ramirez-Franco, J.; Sanchez-Prieto, J.; Torres, M. The Regulation of Synaptic Vesicle Recycling by cGMP-Dependent Protein Kinase Type II in Cerebellar Granule Cells under Strong and Sustained Stimulation. *J Neurosci* **2014**, *34*, 8788-8799.

41. Dingjan, I.; Linders, P. T. A.; Verboogen, D. R. J.; Revelo, N. H.; Ter, M. B.; Van, D. B. G. Endosomal and Phagosomal SNAREs. *Physiol Rev* **2018**, *98*, 1465-1492.

42. Rust, M. B. ADF/Cofilin: A Crucial Regulator of Synapse Physiology and Behavior. *Cell Mol Life Sci* **2015**, *72*, 3521-3529.

43. Wang, S.; Crevenna, A. H.; Ugur, I.; Marion, A.; Antes, I.; Kazmaier, U.; Hoyer, M.; Lamb, D. C.; Gegenfurtner, F.; Kliesmete, Z.; Ziegenhain, C.; Enard, W.; Vollmar, A.; Zahler, S. Actin Stabilizing Compounds Show Specific Biological Effects Due to Their Binding Mode. *Sci Rep* **2019**, *9*, 9731.

44. Yin, S.; Liu, J.; Kang, Y.; Lin, Y.; Li, D.; Shao, L. Interactions of Nanomaterials with Ion Channels and Related Mechanisms. *Br J Pharmacol* **2019**, *176*, 3754-3774.

45. Jakubek, L. M.; Marangoudakis, S.; Raingo, J.; Liu, X.; Lipscombe, D.; Hurt, R. H. The Inhibition of Neuronal Calcium Ion Channels by Trace Levels of Yttrium Released from Carbon Nanotubes. *Biomaterials* **2009**, *30*, 6351-6357.

46. Sidoryk-Wegrzynowicz, M.; Aschner, M. Manganese Toxicity in the Central Nervous System: The Glutamine/Glutamate-Gamma-Aminobutyric Acid Cycle. *J Intern Med* **2013,** *273*, 466-477.

47. Mazánek V; Luxa, J.; Matějková, S.; Kučera, J.; Sedmidubský, D.; Pumera, M.; Sofer, Z. Ultrapure Graphene Is a Poor Electrocatalyst: Definitive Proof of the Key Role of Metallic Impurities in Graphene-Based Electrocatalysis. *ACS Nano* **2019**, *13*, 1574-1582.

48. Ambrosi, A.; Pumera, M. Regulatory Peptides Are Susceptible to Oxidation by Metallic Impurities within Carbon Nanotubes. *Chemistry* **2010**, *16*, 1786-1792.

49. Wu, L.; Liu, L.; Gao, B.; Muñoz-Carpena, R.; Zhang, M.; Chen, H.; Zhou, Z.; Wang, H. Aggregation Kinetics of Graphene Oxides in Aqueous Solutions: Experiments, Mechanisms, and Modeling. *Langmuir* **2013**, *29*, 15174-15181.

50. Chowdhury, I.; Mansukhani, N. D.; Guiney, L. M.; Hersam, M. C.; Bouchard, D. Aggregation and

Stability of Reduced Graphene Oxide: Complex Roles of Divalent Cations, pH, and Natural Organic Matter. *Environ Sci Technol* **2015**, *49*, 10886-10893.

51. Lu, K.; Dong, S.; Petersen, E. J.; Niu, J.; Chang, X.; Wang, P.; Lin, S.; Gao, S.; Mao, L. Biological Uptake, Distribution, and Depuration of Radio-Labeled Graphene in Adult Zebrafish: Effects of Graphene Size and Natural Organic Matter. *ACS Nano* **2017**, *11*, 2872-2885.
52. Lee, C.; Wei, X.; Kysar, J. W.; Hone, J. Measurement of the Elastic Properties and Intrinsic Strength of Monolayer Graphene. *Science* **2008**, *321*, 385-388.
53. Sanchez, V. C.; Jachak, A.; Hurt, R. H.; Kane, A. B. Biological Interactions of Graphene-Family Nanomaterials: An Interdisciplinary Review. *Chem Res Toxicol* **2012**, *25*, 15-34.
54. Zhang, J.; Yang, H.; Shen, G.; Cheng, P.; Zhang, J.; Guo, S. Reduction of Graphene Oxide *via* L-Ascorbic Acid. *Chem Commun* **2010**, *46*, 1112-1114.
55. Zhang, W.; Wang, C.; Li, Z.; Lu, Z.; Li, Y.; Yin, J. J.; Zhou, Y. T.; Gao, X.; Fang, Y.; Nie, G.; Zhao, Y. Unraveling Stress-Induced Toxicity Properties of Graphene Oxide and the Underlying Mechanism. *Adv Mater* **2012**, *24*, 5391-5397.
56. Burkart, J.; Sala, T.; Romanini, D.; Marangoni, M.; Campargue, A.; Kassi, S. Communication: Saturated CO2 Absorption Near 1.6 μm for Kilohertz-Accuracy Transition Frequencies. *J Chem Phys* **2015**, *142*, 191103.
57. Mathew, K.; Sundararaman, R.; Letchworth-Weaver, K.; Arias, T. A.; Hennig, R. G. Implicit Solvation Model for Density-Functional Study of Nanocrystal Surfaces and Reaction Pathways. *J Chem Phys* **2014**, *140*, 084106.
58. Perdew, J. P.; Burke, K.; Ernzerhof, M. Generalized Gradient Approximation Made Simple. *Phys Rev Lett* **1996**, *77*, 3865-3868.
59. Garrity, K. F.; Bennett, J. W.; Rabe, K. M.; Vanderbilt, D. Pseudopotentials for High-Throughput DFT Calculations. *Comput Mater Sci* **2014**, *81*, 446-452.
60. Rasmussen, I.; Pedersen, L. H.; Byg, L.; Suzuki, K.; Sumimoto, H.; Vilhardt, F. Effects of F/G-Actin Ratio and Actin Turn-Over Rate on NADPH Oxidase Activity in Microglia. *BMC Immunol* **2010**, *11*, 44.

## Figures

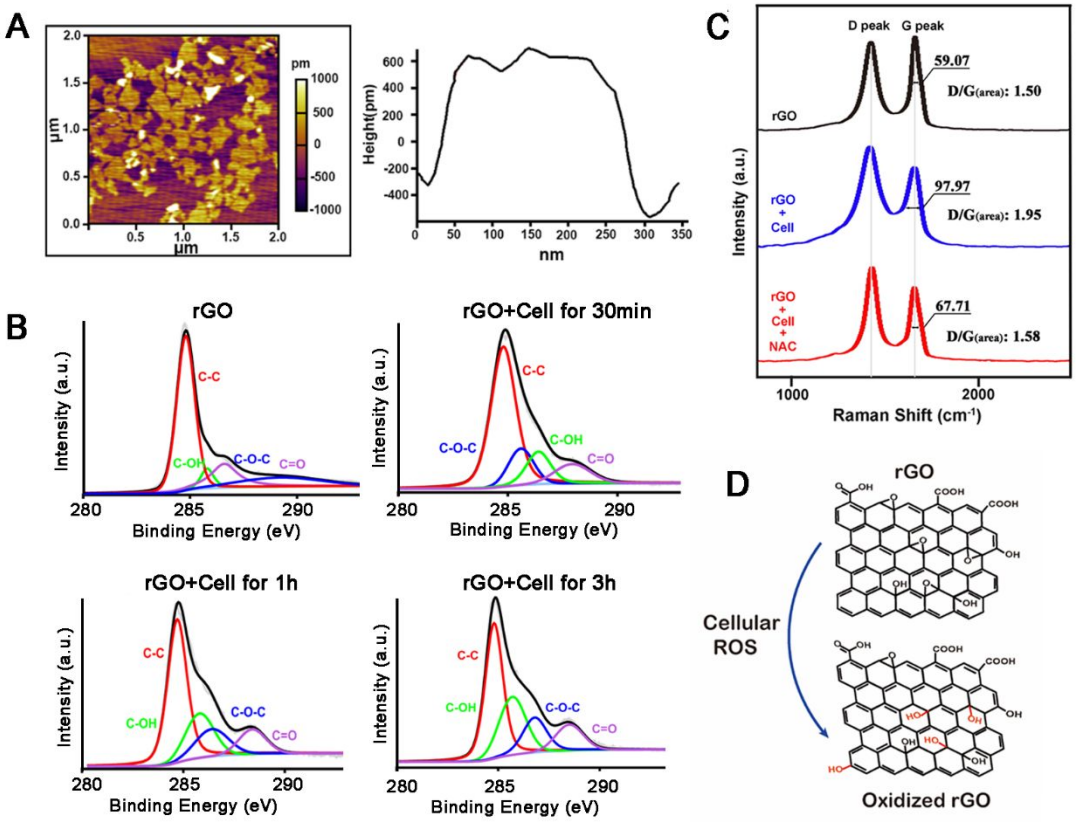


**Figure 1 Characterization of rGO nanosheets.** (A) AFM was used to characterize the surface topography and height of rGO. (B) XPS spectra showing the oxygen-containing functional groups on the rGO surface after culture with PC12 cells for 0, 30 min, 1 h and 3 h. (C) Raman spectra of rGO cultured with PC12 cells for 3 h in the presence or absence of NAC (1 mM). The area ratio of the D peak *vs*. G peak and the FWHMs of the G peak were calculated. (D) Schematic of rGO oxidation by cellular ROS.

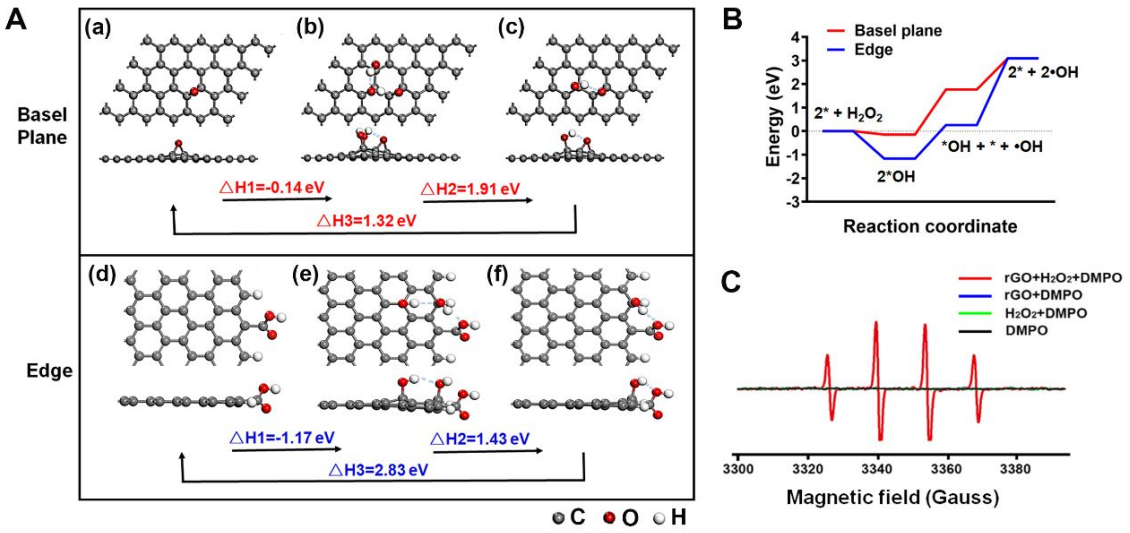


**Figure 2 Oxidation of rGO nanosheets *via* cellular $H_2O_2$.** (A) Side and top views of the rGO surface with one –COC– group (a) and the rGO edge with one –COOH group (d). Two –OH groups were generated due to $H_2O_2$ decomposition (b and e); one –OH group was desorbed (c and f). Energy consumption was calculated within the process. Gray ball: carbon; red ball: oxygen; white ball: hydrogen. (B) Energy profile of the redox reaction for $H_2O_2$ dissociation to •OH. (C) ESR spectra showing •OH formation by $H_2O_2$ and rGO in the presence or absence of $H_2O_2$ (1 mM). DMPO was used as the spin-trapping agent.

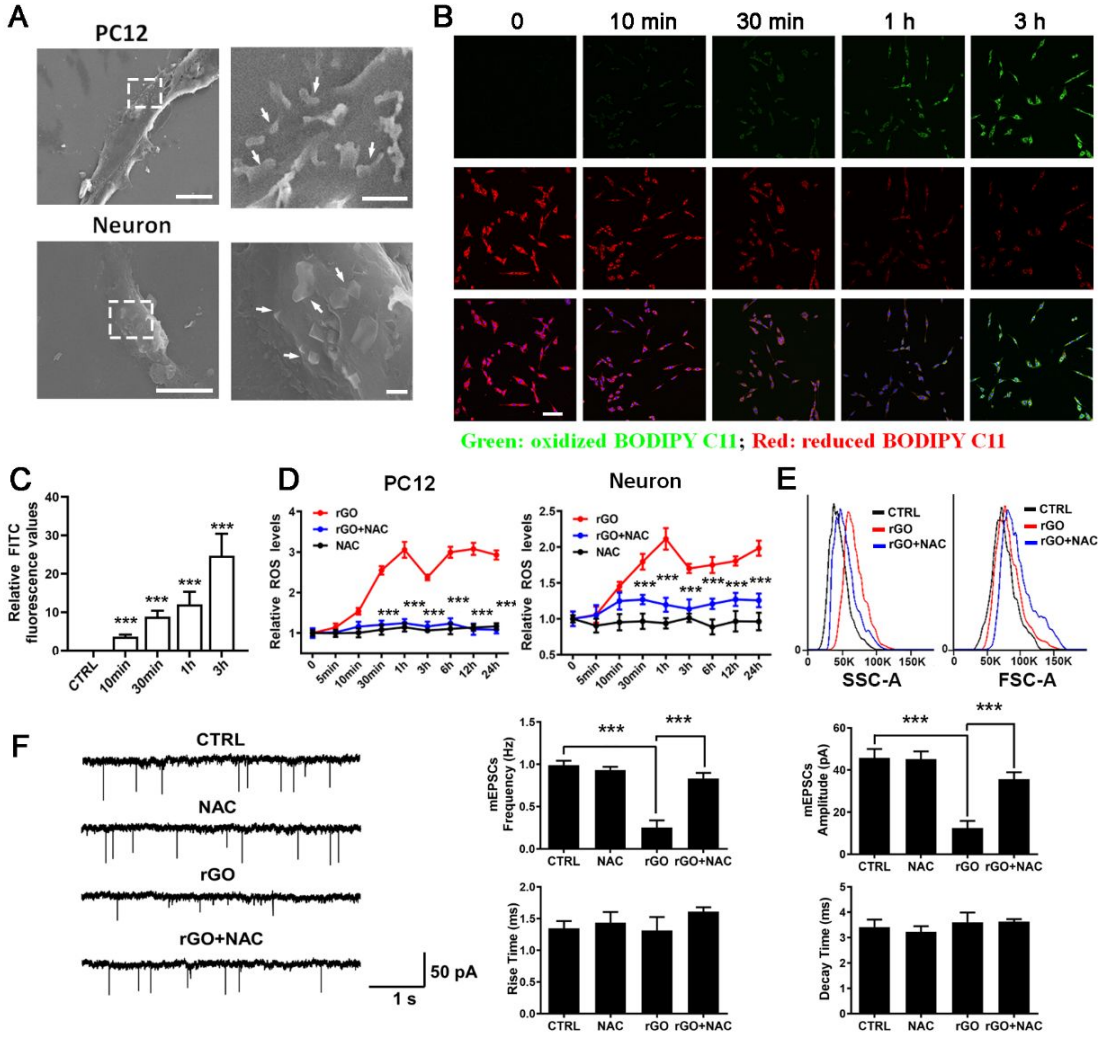


**Figure 3 Interaction between rGO nanosheets and the plasma membrane of neuronal cells.** (A) Representative SEM images showing the interaction of nanosheets with PC12 cells and cortical neurons after treatment with rGO (20 $\mu$g/mL) for 1 h (arrow shows). Scale bar: 10 $\mu$m in main images; 1 $\mu$m in zoomed images. (B-C) Lipid peroxidation in PC12 cells treated with rGO was studied by using the BODIPY 581/591 C11 reagent to visualize the green shift in fluorescence activity in the presence of lipid peroxides. Scale bar: 100 $\mu$m. The lipid peroxidation degrees were quantified *via* FITC fluorescence intensity, $n$ = 10 fields per experimental condition from 3 independent tests. (D) Intracellular ROS levels were detected after PC12 cells and cortical neurons were treated with rGO for various durations. (E) Flow cytometry analysis of SSCs and FSCs in cortical neurons treated with rGO for 3 h in the presence or absence of NAC. (F) Representative

recordings of mEPSCs in cortical neurons treated with rGO for 12 h in the presence or absence of NAC ($n$ = 8 cells from 3 independent experiments). The frequency, amplitude, decay and rise time of mEPSCs were quantified. The results represent the mean ± SD of three independent experiments. ***$p$<0.001 compared with the control group for (C, F) and compared with the rGO group for (D, F).

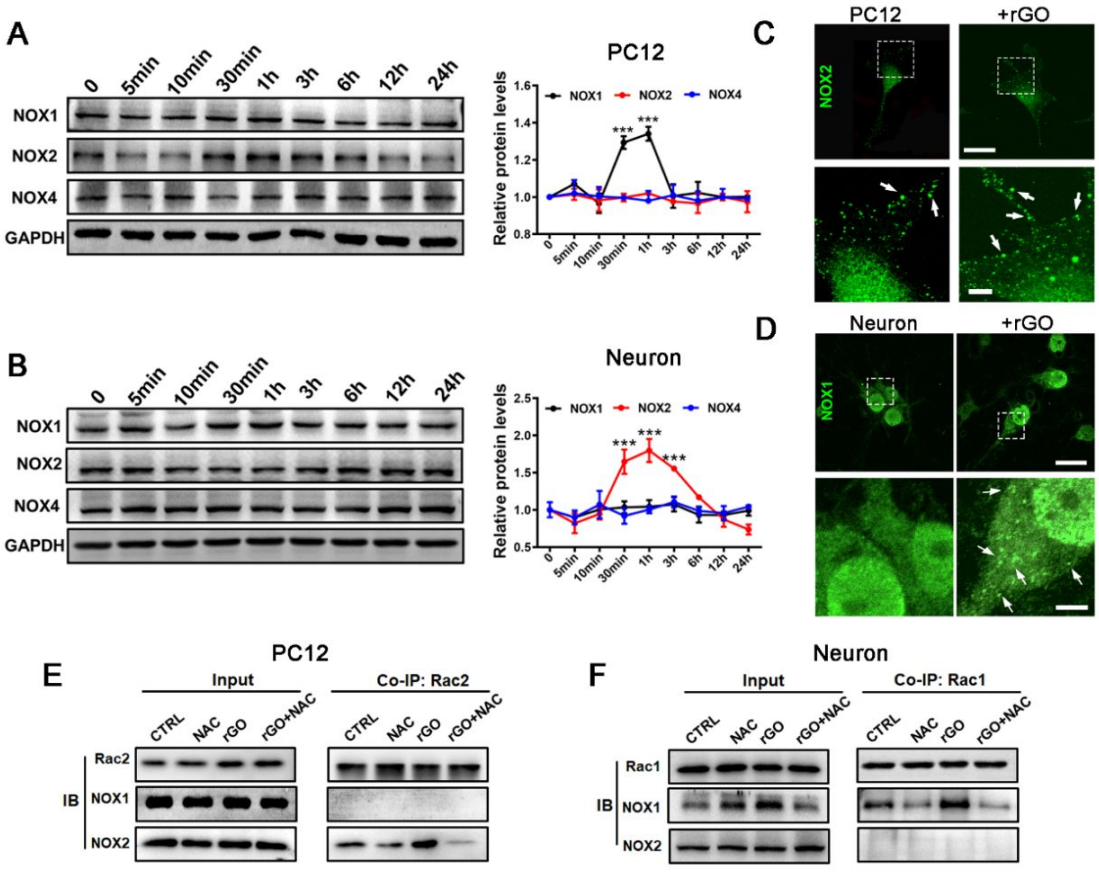


**Figure 4 Oxidized rGO activated NOXs in neuronal cells.** (A-B) Levels of NOX-related proteins were detected *via* western blot after PC12 cells and cortical neurons exposed to rGO. Changes in the levels of NOX1, NOX2 and NOX4 were quantified after normalization to GAPDH. (C-D) Representative images of NOX2 (green) expression and distribution in PC12 cells and NOX1 (green) in cortical neurons with or without rGO treatment (arrow shows). Scale bar: 50 $\mu$m in main images; 10 $\mu$m in zoomed images. (E) Co-IP detected the combination of Rac2 with NOX2 but not with NOX1 in PC12 cells after treatment with rGO for 1 h in the presence or absence of NAC. (F)

Co-IP detected the combination of Rac1 with NOX1 but not with NOX2 in neurons after treatment with rGO for 1 h in the presence or absence of NAC. The results represent the mean ± SD of three independent experiments. ***$p$<0.001 compared with the control group.

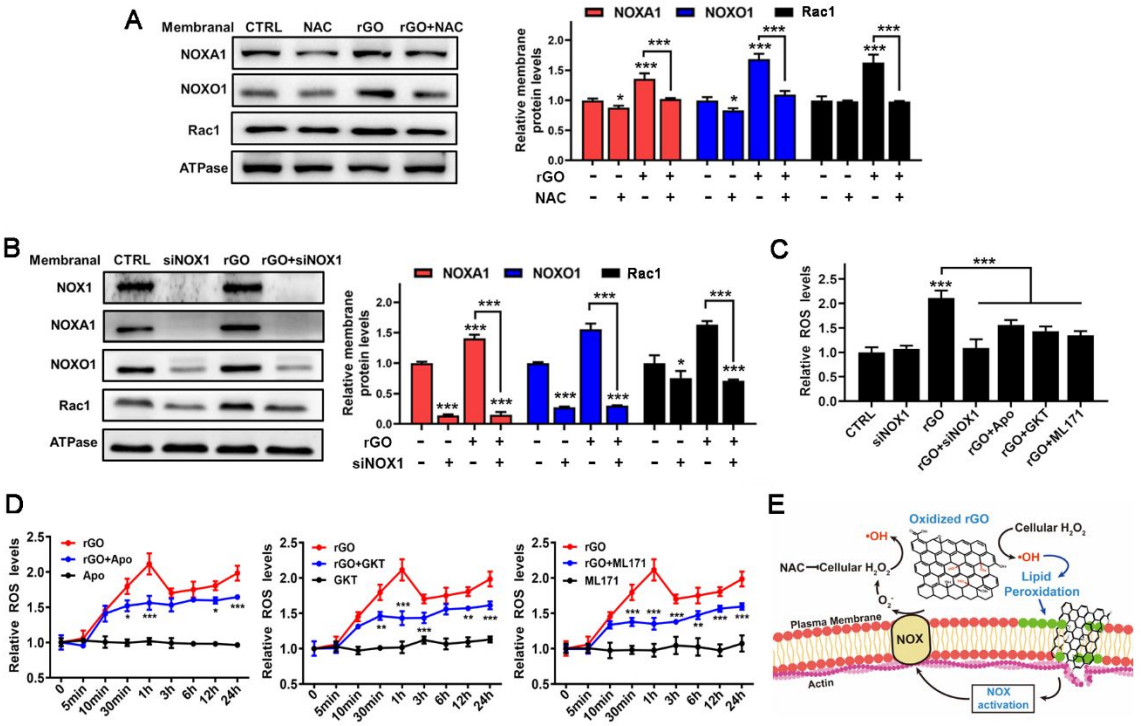


**Figure 5 NOX1 activation is the main source of ROS in cortical neurons.** (A-B) Plasma membrane proteins were isolated to detect NOX1 related proteins translocation after rGO treated with PC12 cells for 1 h in the presence or absence of NAC, or treated with siNOX1-transfected neurons. Changes in the levels of proteins were quantified after normalization to ATPase. (C) Alterations in cellular ROS levels in cells treated with rGO for1 h in the presence of Apo (10 μM), GKT (5 μM) and ML171 (5 μM) and in siNOX1-transfected neurons. (D) Intracellular ROS levels were also detected in neurons treated with rGO in the presence or absence of Apo, GKT and ML171 for various durations. (E) Schematic of oxidized rGO-induced NOXs activation to induce additional ROS generation, leading to intensification of rGO oxidation. The results represent the mean ± SD of three independent experiments. *$p$<0.05, **$p$<0.01, ***$p$<0.001 compared with the control group for (A-C) and compared with the rGO group for (A-D).

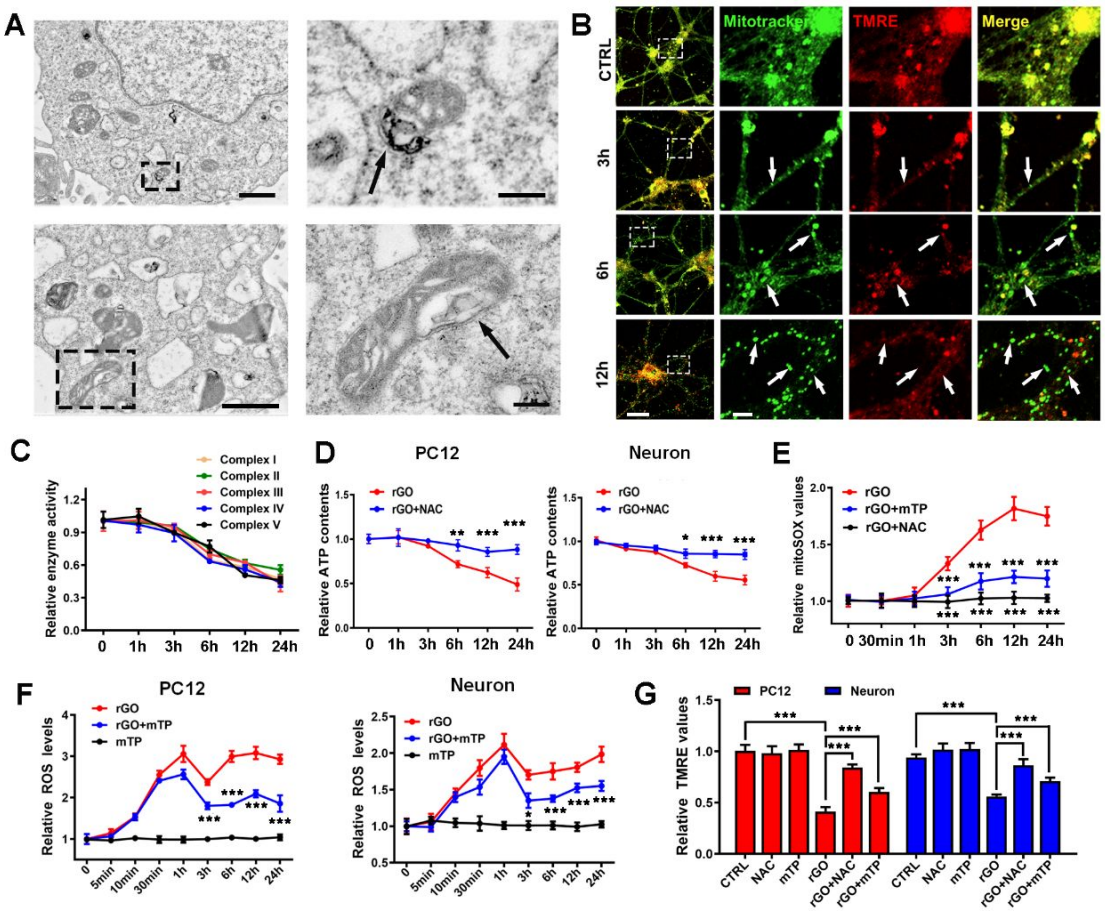


**Figure 6 rGO disturbed mitochondrial structure and function.** (A) TEM images of the interaction between rGO nanosheets and mitochondria in PC12 cells (black arrow shows). Scale bar: 1 $\mu$m in main images; 200 nm in zoomed images. (B) TMRE (red) and MitoTracker (green) fluorescence in cortical neurons after treatment with rGO. The mitochondrion with MMP depolarization were not labeled with TMRE (white arrow shows). Scale bar: 50 $\mu$m in main images; 10 $\mu$m in zoomed images. (C) Enzyme activities of mitochondrial ETC complexes in PC12 cells after treatment with rGO. (D) Cellular ATP contents in PC12 cells and cortical neurons treated with rGO in the presence or absence of NAC. (E) mtROS levels were detected *via* the MitoSOX probe in PC12 cells after treatment with rGO in the presence or absence of mTP (5 μM) and NAC. (F) Cellular ROS levels in PC12 cells and cortical neurons after treatment with rGO in the presence or absence of mTP. (G) TMRE fluorescence in PC12 cells and neurons after treatment with rGO in the presence or absence of mTP and NAC for 6 h. The results represent the mean ± SD of three

independent experiments. *$p$<0.05, **$p$<0.01, ***$p$<0.001 compared with the rGO group for (D-G) and compared with the control group for (G).

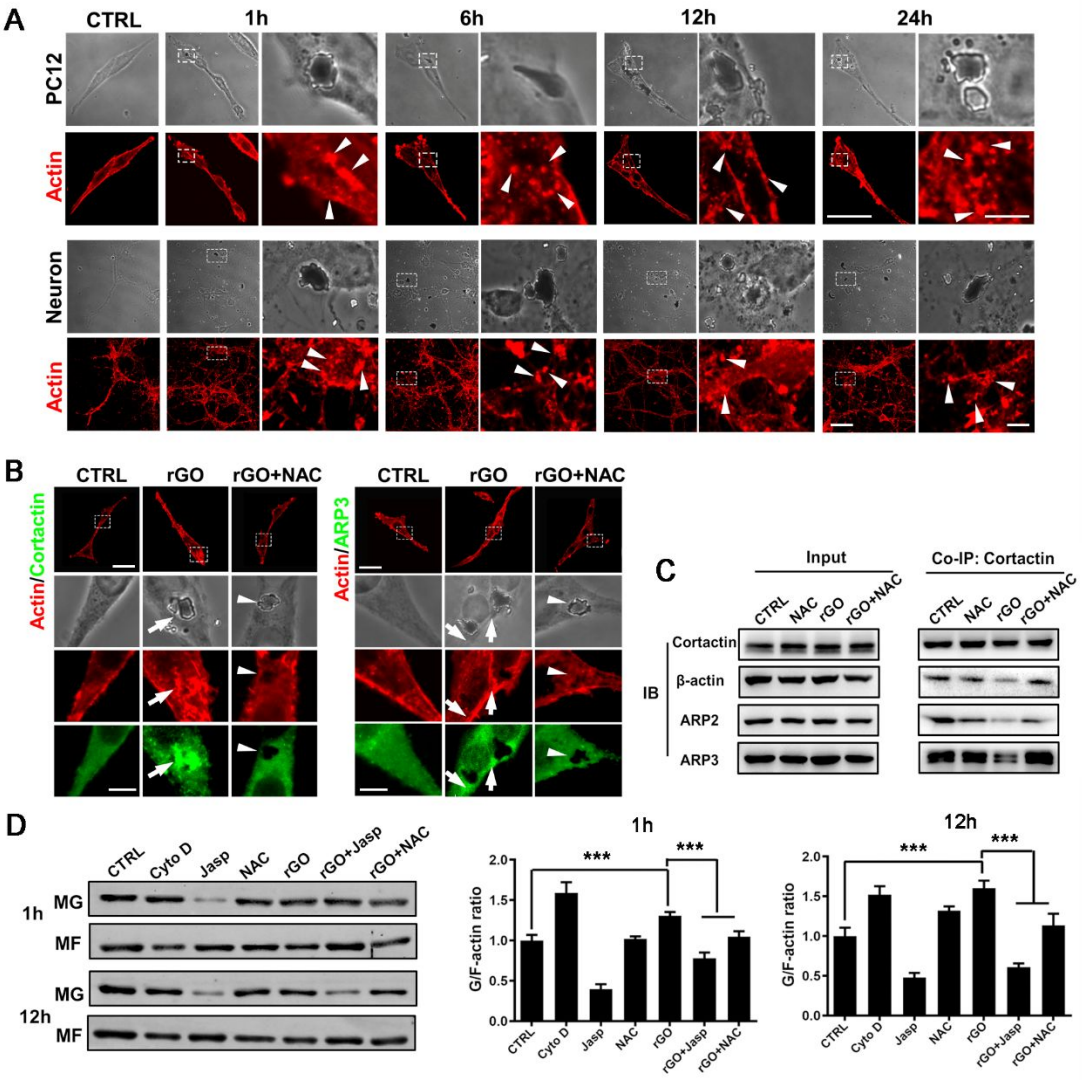


**Figure 7 Oxidized rGO induced actin disturbance.** (A) After PC12 cells and cortical neurons were treated with rGO, actin filaments (phalloidin, red) were found to generate dots around the rGO nanosheets (arrowhead shows). Scale bar: 50 $\mu$m in main images; 8 $\mu$m in zoomed images. (B) After PC12 cells were treated with rGO for 6 h, cortactin and ARP3 were highly recruited around the nanosheets (arrow shows), which could be reversed *via* NAC (arrowhead shows). Scale bar: 25 $\mu$m in main images; 5 $\mu$m in zoomed images (C) Co-IP showed the combination of cortactin with ARP2, ARP3 or β-actin in PC12 cells after treatment with rGO for 6 h in the presence or

absence of NAC. (D) The G/F-actin ratio was detected after cortical neurons treated with rGO for 1 and 12 h in the presence or absence of Jasp (100 nM) and NAC. Cyto D (5 μM) treatment for 2 h was used as a positive control. The results represent the mean ± SD of three independent experiments. ***$p$<0.001 compared with the control group and rGO group.

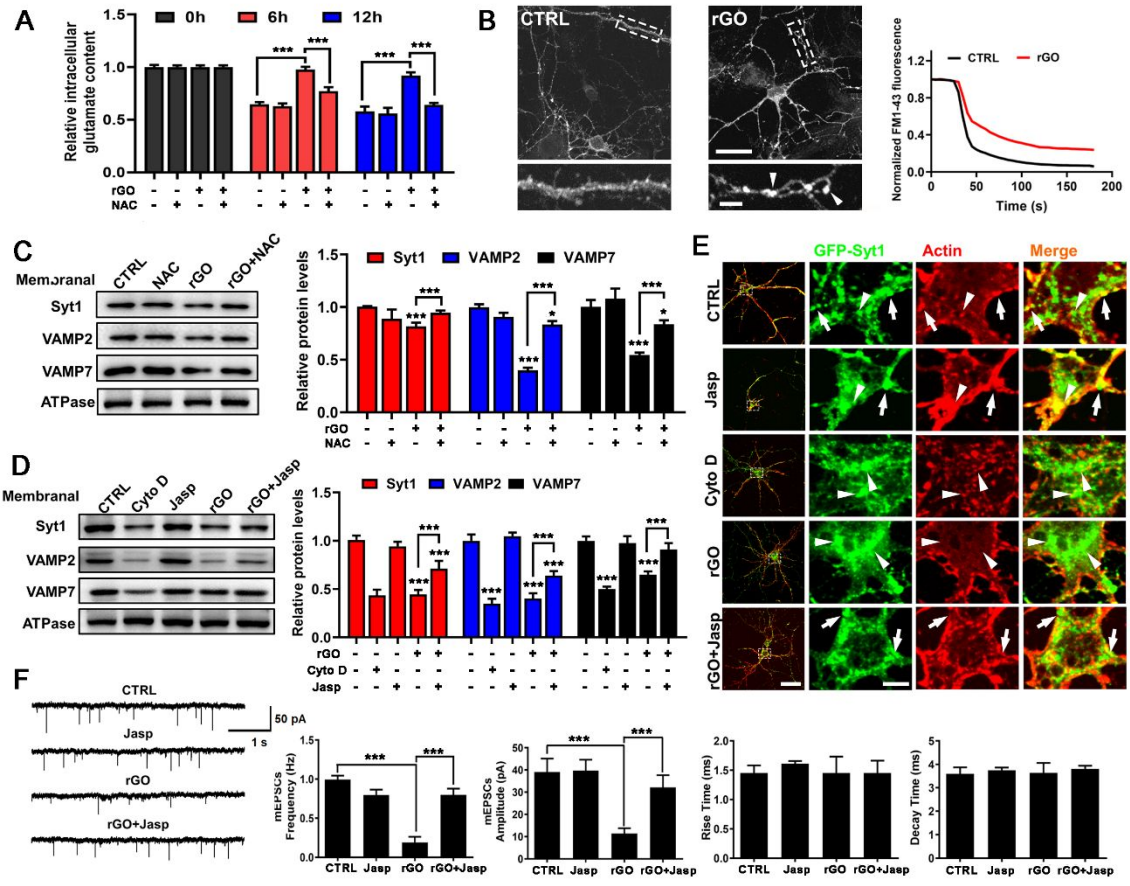


**Figure 8 Actin disturbance mediated oxidized rGO-induced neurotransmission depression.** (A) Relative intracellular glutamate levels were detected in cortical neurons after treatment with rGO in the presence or absence of NAC. (B) Fluorescence image (left) of FM1-43 stained primary neurons after destaining for 1 min in high potassium solution (50 mM) in control and rGO treatment group (arrowhead shows the bright terminal). The traces (right) of synapses from control and rGO treated neurons that undergo FM1-43 destaining were calculated ($n$ = 7 coverslips from 3 independent experiments). Scale bar: 25 $\mu$m in main images; 5 $\mu$m in zoomed images. (C-D) The membrane protein levels of synaptic vesicle-related proteins were detected to evaluate synaptic

docking and fusion after treatment with Cyto D for 2 h or rGO in the presence or absence of NAC or Jasp for 12 h. (E) Colocalization and expression of GFP-Syt1 (green) and F-actin (red) in neurons were detected after treatment according to (D). The arrow shows the GFP-Syt1 containing vesicles dock and fuse with the actin linked membrane, while arrowhead shows the GFP-Syt1 containing vesicles locate in the cytoplasm. Scale bar: 50 $\mu$m in main images; 10 $\mu$m in zoomed images. (F) Patch clamp recordings of mEPSCs in cortical neurons after treatment with rGO for 12 h in the presence or absence of Jasp ($n$ = 7 cells from 3 independent experiments). The frequency, amplitude, decay and rise time of mEPSCs were quantified. The results represent the mean ± SD of three independent experiments. *$p$<0.05, ***$p$<0.001 compared with the control group and rGO group.

**For Table of Contents Only**